Self-healing plasma electrolytic oxidation (PEO) coating developed by an assembly of corrosion inhibitive layer and sol-gel sealing on AA2024

Sajjad Akbarzadeh [a,b], Leonardo Bertolucci Coelho [a,c], Lisa Dangreau [d], Alex Lanzutti [e], Lorenzo Fedrizzi [e], Marie-Georges Olivier [a,d,*]

[a] Materials Science Department, Faculty of Engineering, University of Mons, 20, Place du Parc, 7000 Mons, Belgium
[b] Metallurgy Department, Faculty of Engineering, University of Mons, 20, Place du Parc, 7000 Mons, Belgium
[c] ChemSIN – Chemistry of Surfaces, Interfaces and Nanomaterials, Université libre de Bruxelles (ULB), Boulevard du Triomphe 2, 1050 Brussels, Belgium
[d] Materia Nova Research Centre, 1, Avenue N. Copernic, Parc Initialis, 7000 Mons, Belgium
[e] Department of Chemistry Physics and Environment, University of Udine, Via del Cotonificio 108, 33100 Udine, Italy

ARTICLE INFO

ABSTRACT

The inherent porous structure of PEO coatings is regarded as a drawback for long-term protection. In this investigation, the presence of pores and defects in the PEO coating was exploited as reservoirs for corrosion inhibitors to generate self-healing properties on AA2024. Smart coating systems were fabricated on the PEO layer in which 8-hydroxyquinoline (8-HQ) and benzotriazole (BTA) were employed as corrosion inhibitive layers followed by a sol-gel sealing. The protective performance relies on the mechanical interlocking between the sol-gel coating and the sublayer plus the sealing ability of the sol-gel in the presence of the intermediate layer.

1. Introduction

Aluminum alloys, particularly those in the Al-Cu-Mg system (2xxx series), are widely used in aerospace applications due to their reliable weight-to-strength ratio [1]. Two copper sources in the AA2024 alloy include major elements, represented as Al_6(Cu, Mn, Fe), and S-phase intermetallic particles denoted as Al_2CuMg. While having proper mechanical characteristics, AA2024 has a significant downside which is its susceptibility to localized corrosion [2,3]. The metal surface can be exposed to corrosive electrolytes in any oxide heterogeneity or transient breakdown event because of the weak protective qualities of the passive layer on the S-phase [4]. It is highly suggested to use a surface treatment to reduce its weaknesses [5]. Anodization [6], ion implantation [7], diffusion treatment [8], thermal spraying [9], physical vapor deposition (PVD) [10], chemical vapor deposition (CVD) [11], conversion coatings [12], and PEO [13] are addressed as the most recent surface treatments to improve the corrosion protection performance of aluminum alloys. Due to its eco-friendly qualities and ability to create thick and dense ceramic coatings on light metals, PEO plays a significant part in these processes [14]. For applications demanding wear resistance, PEO coatings are more advantageous than hard anodizing and hard-chrome plating [15].

PEO has been employed to grow an oxide layer with promising corrosion resistance properties on a variety of light alloys, including Al, Ti, and Mg [16–19]. Comparatively greater voltage than anodizing in the PEO process resulted in the occurrence of plasma reactions, species diffusion, and electrochemical reactions at the working electrode. The PEO technique often uses a diluted alkaline water-based electrolyte which makes it more environmentally friendly than anodizing method [20,21]. Many transitory micro-arcs that emerge on the surface substantially raise the temperature and pressure in local areas. The oxide layer is meant to regularly melt and solidify while micro discharges occur over the surface, leading to the assimilation of the oxide layer with the electrolyte components and the development of high-temperature phases [22,23]. As a result, a ceramic layer with enhanced wear, hardness, and corrosion protective properties is constructed. In particular, the inner dense layer and porous outer layer are two sublayers of the PEO coating on aluminum alloys in which having pores and cracks in the porous layer is considered a disadvantage for a long-term protection application [24].

Several surface modifications, including conversion and hydrothermal treatments where the anti-corrosion capabilities might be improved by precipitating low-soluble chemicals, have been proposed to seal the inherent porosity and flaws of PEO coatings [25–27]. Thanks to

---

flexibility, little impact on the environment, and simplicity of production, the use of sol-gel coatings has drawn a great deal of interest [28–32]. Sol-gel layers as a straightforward approach for sealing the PEO porous layer improve the protective performance of the PEO layer owing to its capability of getting into through pores and microcracks [33,34]. However, the effectiveness of sol-gel sealing layers in such systems is determined only by their barrier properties and a self-healing action is missing while cracks and defects provide access to corrosive solutions to reach the substrate. Some scientists proposed that the high porosity of the PEO coating could potentially be thought of as a naturally high-capacity container for the inhibitors [35–38]. Sun et al. [39] introduced and impregnated halloysite particles with BTA to increase the corrosion resistance and grant self-healing potential for a PEO coating; however, the self-healing was limited to the low amount of encapsulated inhibitor. Lamaka et al. [40] proposed the direct loading of corrosion inhibitors, including Ce^{3+} and 8-HQ, into the pores created by the PEO process. It was discovered that the thin sol-gel layer containing Ce^{3+} coated over $MgO/Mg(OH)_2$ withstood corrosion attack and showed self-healing capability. The theory of direct loading of corrosion inhibitors into PEO pores has been additionally confirmed by Yang et al. [41], Gnedenkov et al. [42,43], Mohedano et al. [44], and Ivanou et al. [45] studies.

To the best of the author's knowledge, no investigation has been done regarding the loading of PEO pores on AA2024 substrate with two types of corrosion inhibitors in various concentrations both separately and in combination modes. All investigations have been yet conducted to induce self-healing properties in PEO coatings either produced on Mg alloys or loaded with one distinct type of inhibitor [40–45]. In the present work, the PEO porous layer was loaded with different concentrations (1 g/L, 5 g/L, and 20 g/L) of BTA and 8-HQ corrosion inhibitors in both individual and mixture modes to create the intermediate layer between the sol-gel sealing and the PEO layer. For the mixture case, the ratio between corrosion inhibitors was at first examined in solution mode then this ratio was employed to impregnate the PEO pores in a variety of concentrations. The corrosion inhibition of the 8-HQ and BTA for AA2024 was previously investigated in aqueous solution mode and encapsulated in reservoirs followed by adding to sol-gel or organic coatings [46–50]. It has been demonstrated that corrosion inhibitors like BTA and 8-HQ are extremely favorable in protecting the surface of aluminum alloys. BTA mainly deals with copper-rich intermetallic particles, limiting the cathodic activity. Whereas 8-HQ acts as a mixed-type inhibitor that halts the active sites of aluminum alloys by the creation of a complex chelate [51–53]. The PEO-loaded inhibitor was sealed with a sol-gel layer in which 3-glycidoxypropyltrimethoxysilane (GPTMS) and tetraethoxysilane (TEOS) were the precursors. The TEOS molecule, which has four hydrolysable bonds, is a key component in the formation of sol-gel networks; which joined by the GPTMS moiety, with three hydrolysable branches and one epoxide end group, allows for the pore-filling capability [54]. Therefore, corrosion inhibitors were stored in an intermediate porous layer of the PEO layer under the sol-gel coating.

2. Experiment and methods

2.1. Materials preparation

A 3 cm squared shape of AA2024 having 0.16 cm thickness was used as the substrate with the chemical composition of $\leq$ 0.5% Fe, $\leq$ 0.25% Zn, $\leq$ 0.15% Ni, $\leq$ 0.15% Ti, $\leq$ 0.5% Si, 1.2–1.8% Mg, 3.8–4.9% Cu, 0.3–0.9% Mn, and Al balance. The alloy plates were washed using an ultrasonic bath with acetone for 10 min before the PEO procedure. The coupons were subjected to acid pickling in HNO_3 solution for 30 s at ambient temperature after alkaline etching using NaOH solution at 40 °C for 30 s

For the PEO process, a bipolar power supply (Micronics Systems) was employed to generate a squared pulsed regime with 100 Hz frequency,

30% duty cycle, and 5 A of anodic current for 30 min. The RCQ parameter, which specifies the ratio of applied positive (Q_p) to negative (Q_n) charge amounts throughout one period of the current pulse, was 0.9. The electrolyte comprised KOH and Na_2SiO_3 (Alfa Aesar Co.) at concentrations of 1 g/L and 1.65 g/L, respectively. The electrolyte was enclosed in a double-walled container connected to a cooling device to maintain a temperature below 40 °C [13,55].

The PEO samples were immersed in ethanol-based electrolytes with different concentrations of 1 g/L, 5 g/L, 20 g/L of BTA ($\geq$98.0%, Merck) and/or of 8-HQ (($\geq$98.0%, Sigma-Aldrrich) for 5 min. Then, the samples were placed at room temperature for 1 h prior to the sol-gel application. The PEO samples immersed in BTA solutions at various concentrations are denoted as P-B1, P-B5, and P-B20, the ones dipped in the 8-HQ at different concentrations are abbreviated to P-H1, P-H5, and P-H20 and consequently for the PEO samples loaded with both corrosion inhibitors (BTA + 8-HQ), P-BH1, P-BH5, and P-BH20 abbreviations are employed.

The sol-gel solution contained GPTMS (10% vol/vol) and TEOS (20% vol/vol) in an electrolyte made up of distilled water (60% vol/vol) and ethanol (10% vol/vol). After bringing the pH down to 3 with acetic acid, the solution was mixed for 24 h [56]. All components of the sol-gel solution were purchased from VWR company. By using a KSV Nima dip-coater sol-gel coatings were applied at a withdrawal rate of 100 mm/min followed by being placed at 150 °C for one hour. The PEO sample sealed by the sol-gel is shortened to P-S and the ones which are previously loaded with different corrosion inhibitors in various concentrations are dented as P-B1-S, P-B5-S, P-B20-S, P-H1-S, P-H5-S, P-H20-S, P-BH1-S, P-BH5-S, and P-BH20-S after the sol-gel sealing.

2.2. Methods and procedures

2.2.1. Characterization analyses

Glow Discharge Optical Emission Spectroscopy (GDOES) was implanted by Horiba Jobin Yvon instrument to scrutinize the elemental depth profiles at a power of 40 W and Argon pressure of 650 Pa. Quantum XP software, an Rf-generator (13.6 MHz), a polychromator with 28 acquiring channels, and a conventional 4 mm diameter anode were all featured in the GDOES device. A 0.5 m Paschen Runge polychromator with a nitrogen-purged optical path formed part of the equipment. To get quantitative data, a calibration approach was carried out with SUS (Setting Up Samples) and 30 CRM (Certified Reference Materials) samples. Scanning Electron Microscope (SEM) analysis was conducted by a Hitachi SU8020 instrument equipped with energy dispersive X-ray spectroscopy (EDS) to observe the surficial topography of the PEO-coated samples after loading by various corrosion inhibitors as well as a cross-sectional view of the PEO/intermediate layer/sol-gel coated samples. A Thermoscientific Noran System 7 detector was also installed in the EDS apparatus to provide a comprehensive understanding of the elemental composition of the samples. Fourier Transform Infrared Spectroscopy (FT-IR) was conducted to scrutinize the possible chemical interactions between corrosion inhibitors and the sol-gel network. Accordingly, one could expect to inspect the possibility of chemical interactions in such systems in which the sol-gel sealing and inhibitive layer are present at two distinct layers. Regarding, tiny droplets of the silane coating solutions in which 0.2% wt./wt. of BTA, 8-HQ, and their mixture (BTA+8-HQ) were applied on a Teflon sheet and cured following the steps outlined in Section 2.1 [46]. Then, fine-dried droplets of different sol-gel solutions were collected to perform the FT-IR test using the IRTracer-100 (Shimadzu Co.) instrument within the 650–4000 cm^{-1} wavenumber range. Grazing Incidence X-Ray Diffraction (GIXRD) was performed by Malvern Panalytical Empyrean X-ray diffractometer in θ–θ configuration, employing a copper anti-cathode (λ = 1.54 Å). The percentage area of porosity evaluation of the PEO samples after loading with various corrosion inhibitors was done by ImageJ software. There are certain basic limitations to the porosity evaluation approach used in this study that should be considered. First, the quality and magnification of SEM images are important factors in correctly

determining porosity. The accurate identification and measurement of pores might be hampered by low-resolution pictures or insufficient magnification. Second, it may be challenging to discern between real pores and artifacts in SEM images because of artifacts like charging, staining, or beam damage that can alter the look of the coated surface. Thirdly, choosing a suitable threshold value might be difficult since the thresholding and segmentation procedure in ImageJ relies on individual opinions. The surface roughness of PEO coatings may hinder the precise identification and measurement of individual pores. Although these restrictions exist, essential steps were taken to lessen their effects and guarantee the accuracy of the porosity measurements. At least two calculations were carried out for each sample with the magnification of 400x, using an 8-bit filter in ImageJ software. To do this, the automatic threshold was employed by varying the threshold values, confirming the consistency of the porosity measurements within an acceptable range. The measurement error was estimated by performing replicate measurements on different images, followed by calculating statistical measures such as standard deviation.

2.2.2. Electrochemical exploration

The dual barrier/active performance of coated samples was investigated by Electrochemical Impedance Spectroscopy (EIS) in a simulated aggressive electrolyte via BioLogic SP-300 instrument. Moreover, for the mixture case of the inhibitive layer, the various ratios between the 8-HQ and BTA inhibitors examined by EIS (firstly at 1000 ppm inhibitor concentration) included: 0 and 1000 ppm, 700 and 300 ppm, 500 and 500 ppm, 300 and 700 ppm, and 1000 and 0 ppm; in 0.1 M NaCl solution. The inhibition efficiency of various ratios of corrosion inhibitors was calculated by Eq. 1 [57,58] and summarized in Table 1.

$$\eta = \frac{R_{t,\ i} - R_{t,b}}{R_{t,\ i}} \times 100\% \tag{1}$$

where $R_{t,i}$ and $R_{t,b}$ represent the total resistance (the sum of film resistance (R_{film}) and charge transfer resistance (R_{ct})) in the presence and absence of inhibitors, respectively. Resistance values were obtained by EIS fitting with the electrical equivalent circuit depicted inside of the Nyquist diagram in Fig. 1.

Accordingly, various intermediate layers in the mixture mode (1 g/L, 5 g/L, and 20 g/L in ethanol solution) were prepared based on the optimum ratio resulting from the EIS tests on the substrate. The conventional three-electrode configuration in which platinum was an auxiliary electrode, Ag/AgCl/KCl (+197 mV/SHE) as the reference electrode, and bare/coated panels (AA2024 substrate in solution mode examination) as working electrodes were employed. The EIS findings were achieved using a sine wave fluctuation with a peak-to-peak amplitude of 10 mV within the 100 kHz to 100 mHz frequency domain. The exposed surface area of the coupons to the aggressive solution was 1.0 cm^2, and at least two measurements were performed for each set of samples at any immersion period to test the repeatability of the electrochemical data. To achieve all electrochemical parameters contributing to the corrosion phenomenon, the EIS outcomes were curve-fitted using the most suitable electrical equivalent circuit (EEC) in the ZView software framework. The resistance of charge transfer, PEO layer, sol-gel coating, and

electrolyte was abbreviated to R_{ct}, RP, R_{SG}, and R_e, respectively. Any surface is not an ideal interface due to heterogeneity and roughness, which is why the constant phase element (CPE) was chosen to clarify the EIS results instead of an ideal capacitor determined by Eq. 2 [59].

$$Z_{CPE} = \left[\frac{1}{Y_0 \ (i\omega)^n} \right] \tag{2}$$

where Y_0 is the admittance of CPE and n is the frequency dispersion factor whose domain is 0–1 defining the ideality of the system in terms of being pure resistance (0) or pure capacitance (1). The CPE component of the double layer, PEO, and sol-gel is denoted as CPE_{dl}, CPE_p, and CPE_{SG}, respectively. The presence of the sol-gel along with the intermediate layer inside of the porous PEO layer led to the presence of a mixed region represented as R_{mix} and CPE_{mix} in the employed EEC.

A cut-edge set-up with the coating systems was also considered, in which specimens were mounted in epoxy resin (EpoFix). Scanning Vibrating Electrode Technique (SVET) was carried out via Applicable Electronics (AE) equipment to investigate the dual barrier/active properties of the cross-sections. Prior to testing, mounted samples were mechanically polished with sandpapers up to 2400 grit size followed by covering with 3 M™ Scotchrap™ 50 tape in a way that 2.3 mm^2 was left unmasked. The platinum/iridium SVET probe with ~20 μm diameter was platinized in 1% (wt./wt) lead (II) acetate and 10% (wt./wt) platinum chloride solution for capacitance increase. Then, the SVET calibration was conducted based on the instruction manual of the instrument for 15 mM NaCl solution with 604 Ω cm electrical resistivity. The vibration frequency, vibration amplitude, and probe distance from the exposed surface area were 80 Hz, 40 μm, and ~150 μm, respectively. In order to guarantee the consistency of the results, two samples of each kind were scanned with 31 × 31 grid points at the cut-edge exposed region.

3. Results and discussion

3.1. GIXRD test

Fig. 1 displays the GIXRD patterns of the PEO coating produced on AA2024. PEO coatings on aluminum alloys are typically made of α-Al$_2$O$_3$ and γ-Al$_2$O$_3$, while other studies have documented PEO layers made from amorphous alumina [60]. The oxide-forming process during the initial stages of PEO is comparable to anodic oxidation. Due to the development of plasma channels, when the micro arcing begins, the temperature rises quickly resulting in a transformation of the initial oxide layer into the metastable γ-Al$_2$O$_3$ [61]. Interestingly, greater current densities or longer oxidation periods enable the transformation of γ-Al$_2$O$_3$ into α-Al$_2$O$_3$ [62,63]. The GIXRD in Fig. 1 illustrates some intense peaks ascribed to γ-Al$_2$O$_3$ along with some shoulders of Al substrate. Moreover, the presence of some copper-based phases such as CuO.69Mg1.31Si$_2$O$_6$ (JCPDS card no: 00–021–0154) and Cu$_2$O (JCPDS card no: 00–005–0667) confirmed the EDS findings, referring to the emergence of the copper oxide over the PEO surface.

3.2. FT-IR analysis of direct doping of inhibitors to the sol-gel coating

The sol-gel precursors, such as GPTMS and TEOS, can undergo hydrolysis and condensation reactions in the presence of water and ethanol. During these reactions, silanol groups (hydroxyl groups (OH$^-$) of the sol-gel precursors) can react with each other, leading to the formation of siloxane bonds (Si-O-Si) [64,65]. The hydrolysis and condensation processes might possibly be impacted by the presence of BTA and 8-HQ in the system. FT-IR analysis of sol-gel with and without BTA, 8-HQ, and BTA+ 8-HQ was carried out to see the impact of corrosion inhibitor moieties on the sol-gel network development (Fig. 2). The asymmetric and symmetric stretching vibrations of the Si-O-Si bond have appeared at 1025 and 791 cm^{-1} wavenumbers,

Table 1
The corrosion inhibition efficiency of the substrate after 72 h immersion in 0.1 M NaCl electrolyte with/without different ratios of BTA and 8-HQ (total concentration of 1000 ppm).

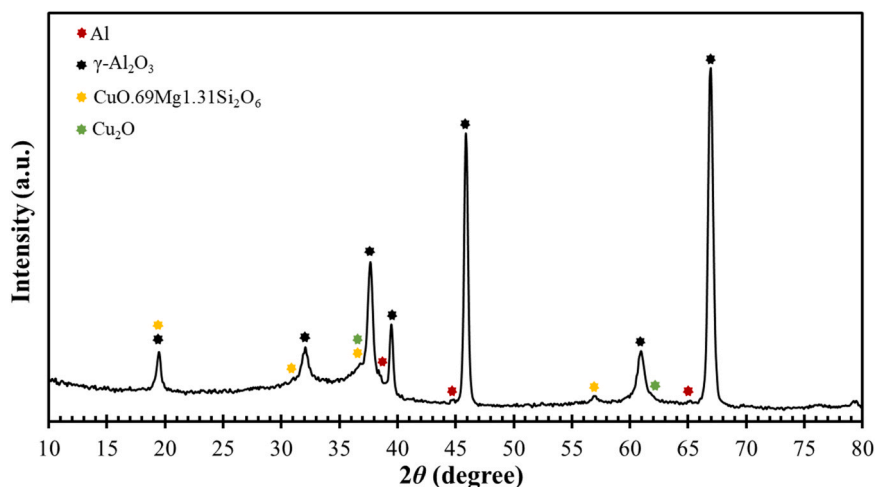| Sample	Blank	BTA 1000	8-HQ 300 -BTA 700	8-HQ 500 – BTA 500	8-HQ 700 - BTA 300	8-HQ 1000
The inhibition efficiency (%)	-	41	39	71	93	20

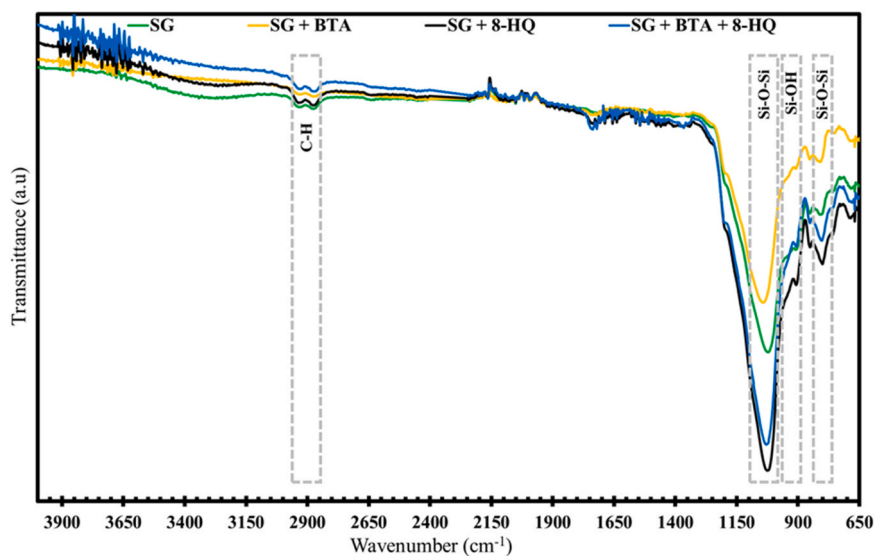**Fig. 1.** GIXRD pattern of the PEO coating on AA2024 substrate.

Fig. 2. FT-IR curves of sol-gel coating doped with BTA and 8-HQ corrosion inhibitors.

respectively [66]. The sharp peak of Si-O-Si at roughly 1025 cm^{-1} wavenumber demonstrates that the silica network was formed by condensation and hydrolysis reaction in sol-gel solutions. It's noteworthy to point out that the ladder-like structure of the sol-gel could be mostly attributed to the shoulder at 1184 cm^{-1} [67]. The Si-O-Si signal was altered by the addition of the corrosion inhibitors as compared to the neat sol-gel spectra. As it could be comprehended, BTA interfered with the sol-gel network formation (decreasing the Si-O-Si peak); however, 8-HQ could facilitate the sol-gel network evolution as the Si-O-Si signal was intensified. This outcome is in parallel with previous studies where BTA and 8-HQ were implemented into the sol-gel coatings [46,68]. Therefore, no matter the positive and negative impact of corrosion inhibitors on the sol-gel development coating, the chemical interactions are not quite far-fetched when sol-gel is applied to the PEO coating loaded with corrosion inhibitors. It most likely results from the presence of functional groups in BTA and 8-HQ, such as amino and hydroxyl groups, which may react with other reactive sites in the sol-gel coating. Amino groups could take part in condensation processes with hydroxyl groups from the sol-gel precursors, generating covalent bonds and chemically integrating into the sol-gel matrix. Similar condensation reactions might occur between the hydroxyl groups in 8-HQ and the reactive species in the sol-gel coating [69,70]. As the GIXRD test was

clarified, plenty of copper-based products were formed over the PEO layer, leading to the formation of bonds with BTA. Such interactions of copper oxide substrates with solutions containing benzotriazole have been studied previously [71,72].

3.3. EIS in solution mode

In order to get the optimum ratio of the inhibitors, the EIS test was conducted with 1000 ppm of inhibitive species in 0.1 M NaCl solution. The Nyquist and Bode plots of the substrate after 72 h immersion in various inhibited solutions are exhibited in Fig. 3. Enlargement of the semi-circle diameter in the Nyquist diagrams illustrated the improvement of the corrosion resistance properties of the substrate in any kind of inhibited electrolyte. Specifically, the Nyquist diagrams reported the highest anti-corrosion performance in the electrolyte containing 8-HQ 700 – BTA 300 in 0.1 M NaCl, as it had the greatest semi-circle diameter. Meaning that, in the ratio of 8-HQ/BTA: 7/3, a synergistic effect of the inhibitors was taken place which might produce a protective layer over the anodic and cathodic sites of the AA2024 alloy. Furthermore, the low-frequency impedance in the Bode diagrams corroborated the fact that 8-HQ 700 – BTA 300 had superior protective characteristics. The phase diagram of the substrate was broadened by using inhibitors,
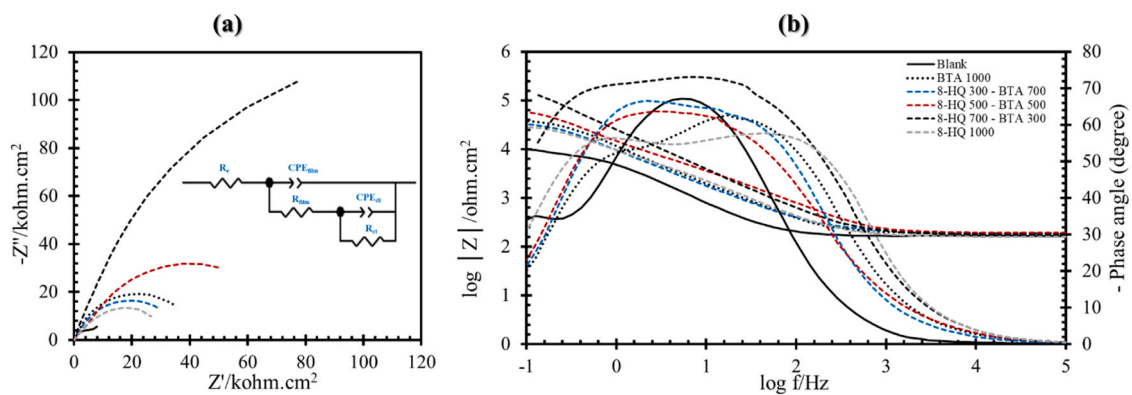
Fig. 3. The electrochemical response of the substrate after 72 h exposure to 0.1 M NaCl in the presence or absence of 1000 ppm corrosion inhibitors in various ratios in the form of Nyquist (a) and Bode (b) diagrams.
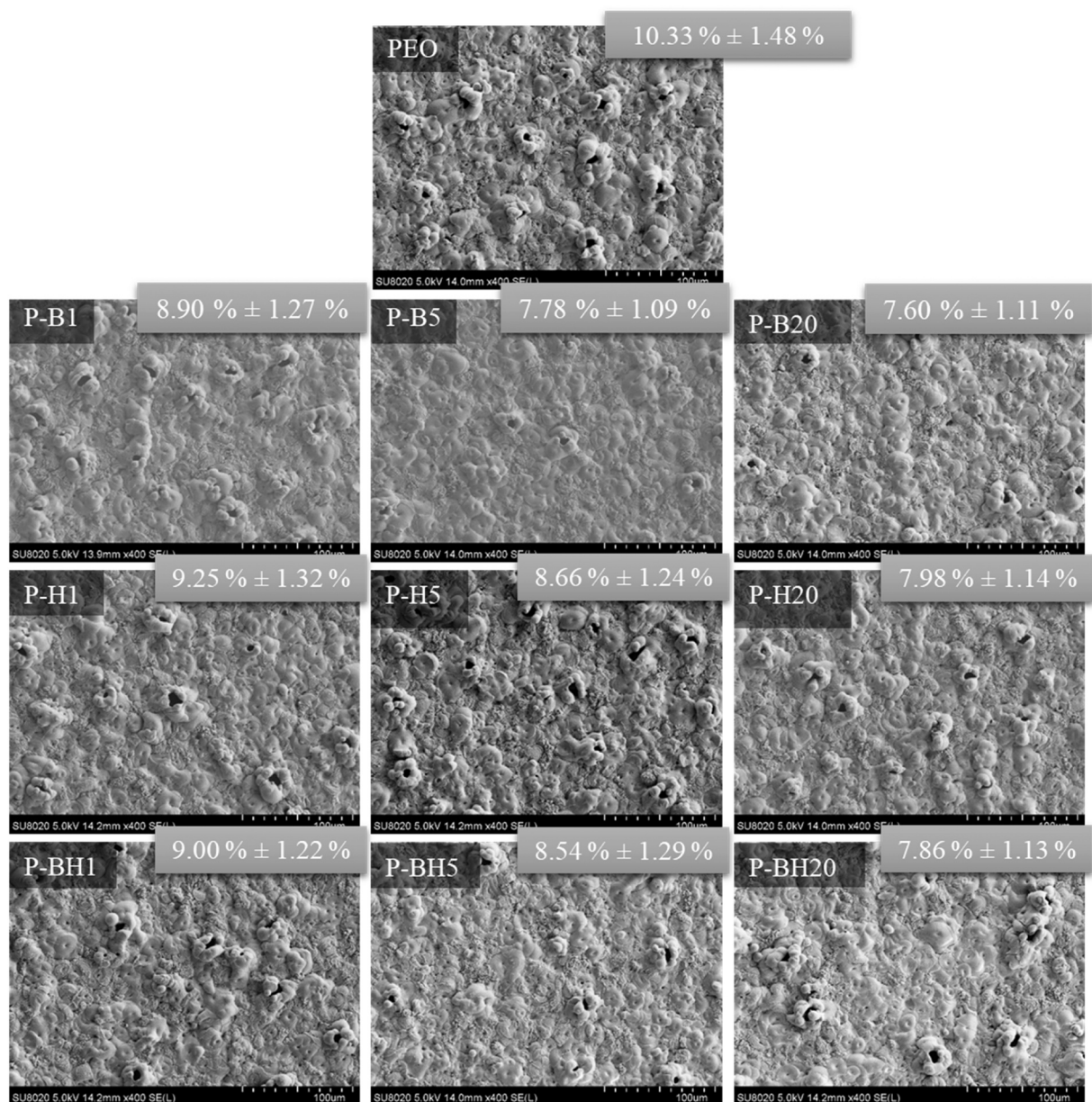

Fig. 4. Surface topography and percentage area of porosity evaluation of the PEO sample after loading with various types of inhibitive layer.

particularly in the 8-HQ 700 – BTA 300 test, which had a more pronounced time constant at 100 mHz. The activity of BTA is primarily restricted to the Cu-rich intermetallic particles, whereas 8-HQ impacts the aluminum matrix due to its chelating capabilities. Adsorption of the inhibitive molecules and complexes consisting of both BTA and 8-HQ corrosion inhibitors, followed by the construction of a layer across the substrate, could hinder the redox reactions. Even though BTA is typically described as a cathodic inhibitor, experiments with the electrochemical micro-cell disclosed that it also influences anodic processes, extending the passive zone of AA2024 [50]. Additionally, the polarization results proved that 8-HQ molecules broadened the passive region of AA2024 [73]. The activation energy of the corrosion process may have increased due to the complex formation between Al^{+3} and 8-HQ molecules [74]. In the presence of both corrosion inhibitors, the galvanic coupling responsible for the corrosion process of AA2024 is significantly restricted, which is not the case when the inhibitors are used separately. Besides, it is well-documented that the E_{corr} shifts in the cathodic direction, leading to a lower chance that pits may develop [75]. The highest inhibition efficiency (93%) was found in a system containing the 8-HQ 700 – BTA 300 inhibitor mixture in the saline solution. Consequently, the ratio of 8-HQ/BTA was selected to be at 7/3 for the inhibitive mixture layer of the PEO/intermediate/sol-gel coating system.

3.4. The SEM observation of PEO-coated samples loaded with inhibitors

3.4.1. Top-view observation

The surface morphology of the PEO specimens after dipping in different inhibitive solutions was visualized by SEM images in Fig. 4. The continuous melting and forming of the oxide layer during the PEO procedure is what gives the PEO layer its distinctive porous features. Numerous pores whose diameters are between 1 and 10 μm established haphazardly in the PEO layer because of the occurrence of the dielectric breakdown and accordingly sparks initiations. The average porosity (which represents the percentage of the total surface area that contains porosity) of the PEO samples was calculated via ImageJ software, and the obtained values are placed at the corner of each image. The higher the concentration of the inhibitive layer, the lower the porosity, regardless of the type of inhibitor layer. Interestingly, the benzotriazole inhibitive layer could reduce the porosity more than the hydroxyquinoline-based one. It might stand to reason that the former is more likely to deposit over the surface. In contrast, the latter is more intended to penetrate through the pores and cracks to mainly act on the aluminum matrix. All in all, in both types of the inhibitive layer, one could expect that the deposition over the PEO surface takes place along with the diffusion into the pores.

EDS elemental maps of PEO coatings loaded with 20 g/L of various corrosion inhibitors are displayed in Fig. 5. In each example, copper and
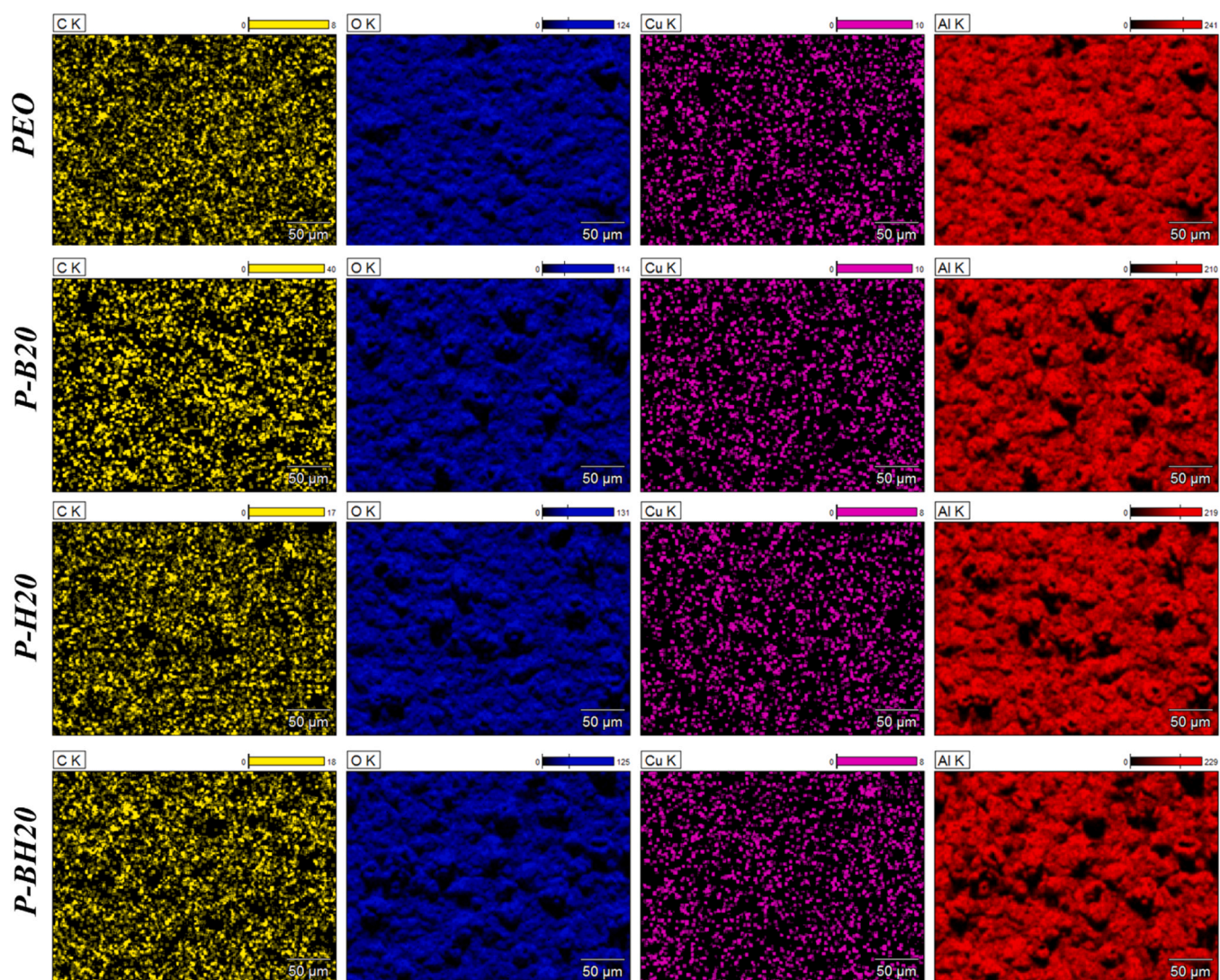

Fig. 5. EDS maps of PEO coating after loading with 20 g/L of BTA, 8-HQ, and BTA+ 8-HQ corrosion inhibitors.

aluminum are perceived on the PEO surface and to be coming from the AA2024 substrate. The emergence of copper oxide over the PEO surface could be considered as a preferential site for BTA to adsorb while 8-HQ acts on the aluminum matrix. The presence of carbon over the PEO surface may refer to contamination during either preparation or handling of the sample. By looking at the scale bar of the C element along with its map, the C amount was enhanced after incorporating corrosion inhibitors thanks to their organic nature. This increment was the uttermost for the P-B20, confirming the hypothesis of BTA precipitation over the PEO surface. For P-H20, the content of C was also increased but not as much as P-B20 as 8-HQ intended to ingress through the PEO cracks and pores.

3.4.2. Cross-section images

The cross-section images of PEO coatings after loading with 20 g/L of BTA, 8-HQ, and BTA+ 8-HQ were exhibited in Fig. 6. The complex and porous structure of the PEO coating brought about various thickness values in which 12.81 ± 4.6, 13.35 ± 4.9, 12.94 ± 4.2, and 13.18 ± 5.1 were attributed to the PEO, P-B20, P-H20, and P-BH20, respectively. Although a slight enhancement in the coating was reported after the application of an inhibitive layer particularly with the one having BTA, the inherent disordered porous shape of the PEO coating could also be misleading for thickness determination. All in all, the coating thickness of the PEO coating remained almost unchanged after loading with the corrosion inhibitive layer even after introducing the highest content of the corrosion inhibitors.

3.5. SEM illustration of PEO/inhibitive layer/sol-gel coating systems

Fig. 7 shows cross-section images coupled with EDS mappings of coating systems consisting of PEO/inhibitive layer/sol-gel system. For the PEO sample, as coatings obtained upon an oxidation process in the silicate solution, the presence of Al, O, and Si could be expected, whereas the C element originated from the permeation of embedding resin into the pores and cracks during sample mounting. After application of the sol-gel layer (P-S sample), pores and any coating deficiencies could be sealed as confirmed by tracing the Si element in the EDS mapping. Therefore, there are no pores, cracks, and any other free volumetric spaces left and available for the embedding resin to diffuse through the sample. The reliable sealing ability of this type of sol-gel coating (mixture of TEOS and GPTMS precursors having four and tree hydrolysable groups, respectively) was also investigated elsewhere [76–78]. As no trace of embedding resin (by C mapping) could be noticed in such a sol-gel sealed system, the presence of C (EDS mapping) in the PEO/intermediate layer/sol-gel coating systems is caused by the organic compounds throughout the porous network structure of the PEO layer. In other words, the sol-gel is able to seal the pores of the PEO layer on the AA2024 substrate, unless it was filled previously by another material, namely the inhibitive layer. The nitrogen content of the inhibitor species can not be detected by EDS due to its low atomic number. By thoroughly looking at the EDS mapping, it was found that the higher the concentration of the inhibitive layer, the lower the sol-gel sealing. While the presence of an inhibitive layer resembling an encapsulated inhibitive reservoir alongside the sol-gel sealing could be observed.

3.6. GDOES analysis

The GDOES analysis (Fig. 8) was performed to illustrate the elemental depth profile of Si, O, C, and Al in coated samples. Nitrogen involved in the chemical formula of 8-HQ and BTA can not be detected by using this technique due to the air infiltration (rich in N) in the porous structure of the PEO layer. The elemental profiles of Si and C signals are magnified by 60 and 40, respectively. Two regions can be found in certain PEO coating including the porous region and dense layer. The relatively strong intensity of O and low signal of Al from 0 μm to 7 μm is related to the porous region of the PEO layer. From ~ 7–15 μm, the exponential decrease in intensity of the O signal along with a more pronounced response of Al attributed to the dense layer of the PEO layer. At a depth higher than 15 μm, the Al response becomes dominant, and the rest can barely be detected, illustrating the substrate response [79]. As TEOS and GPTMS were utilized in the sol-gel formulation, the response of C and Si elements was enhanced noticeably after the application of sol-gel. All sealed PEO samples indicate that sol-gel lies partially in the porous region and substantially somewhere between the
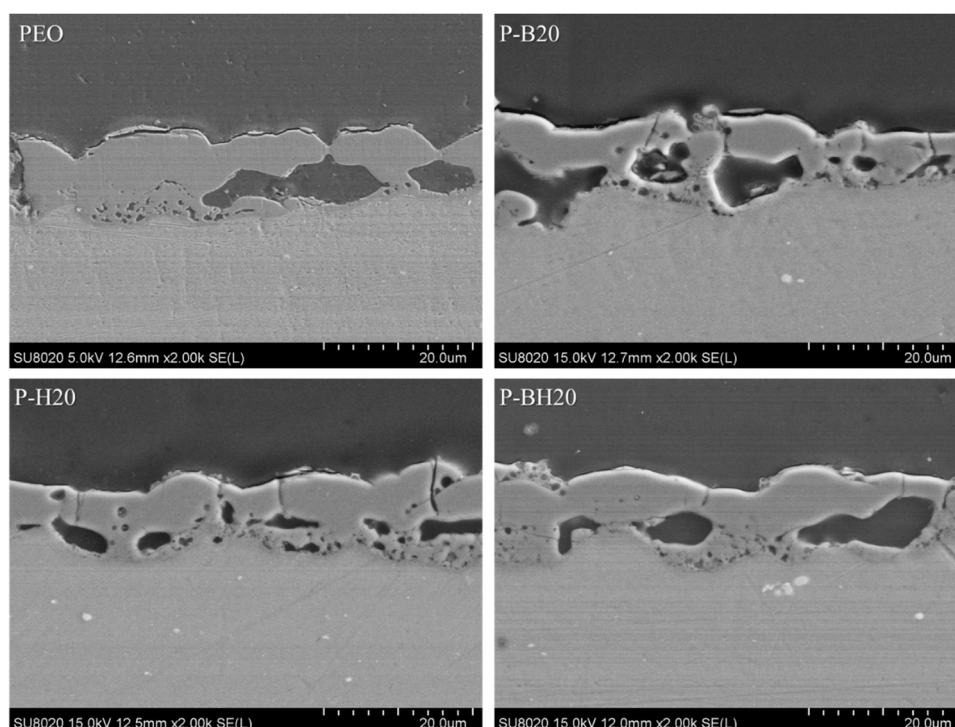

Fig. 6. Cross-section visualization of PEO coated samples after loading with 20 g/L inhibitive layer.
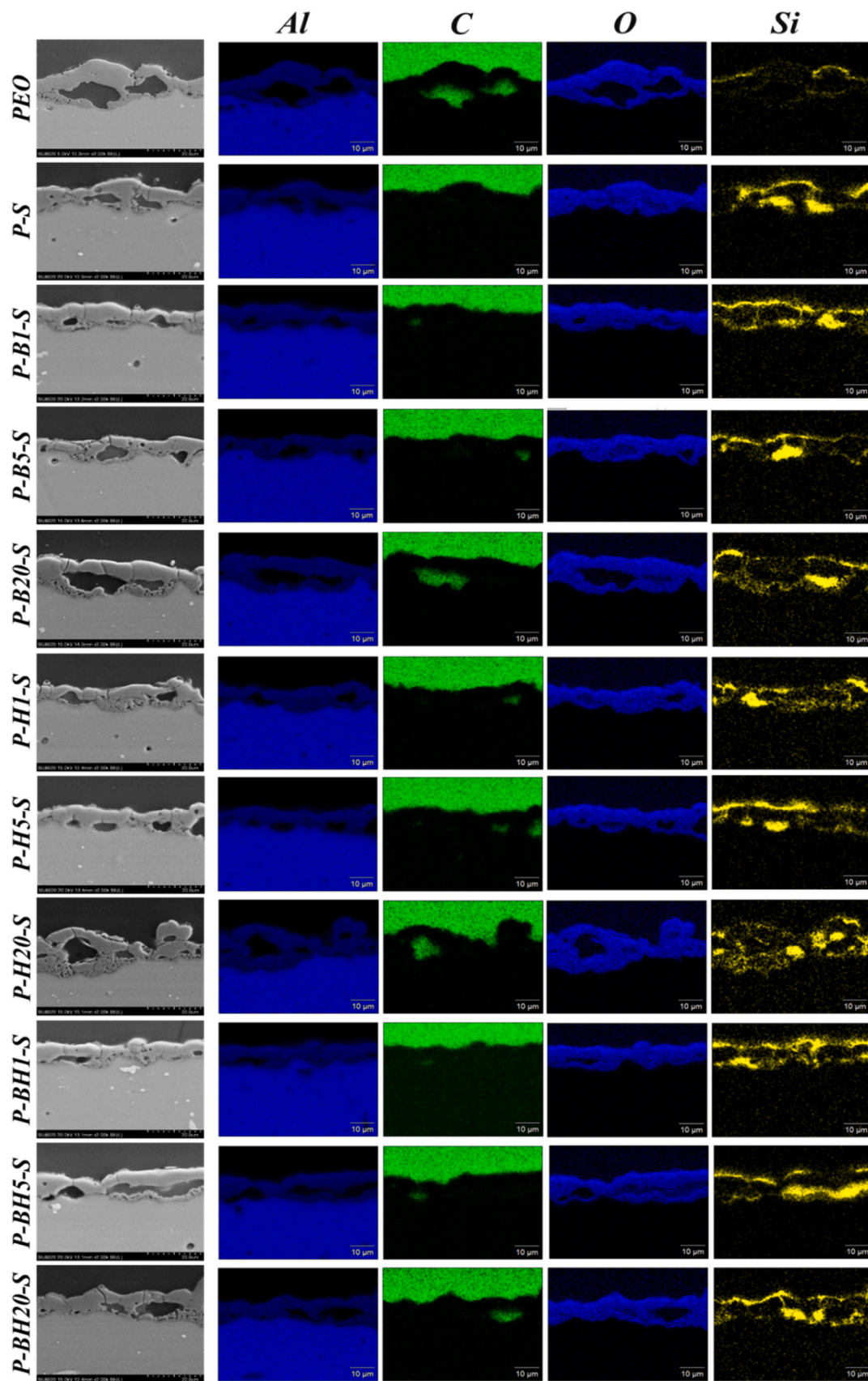
Fig. 7. Cross-sectional SEM images plus EDS mappings of various coating systems.
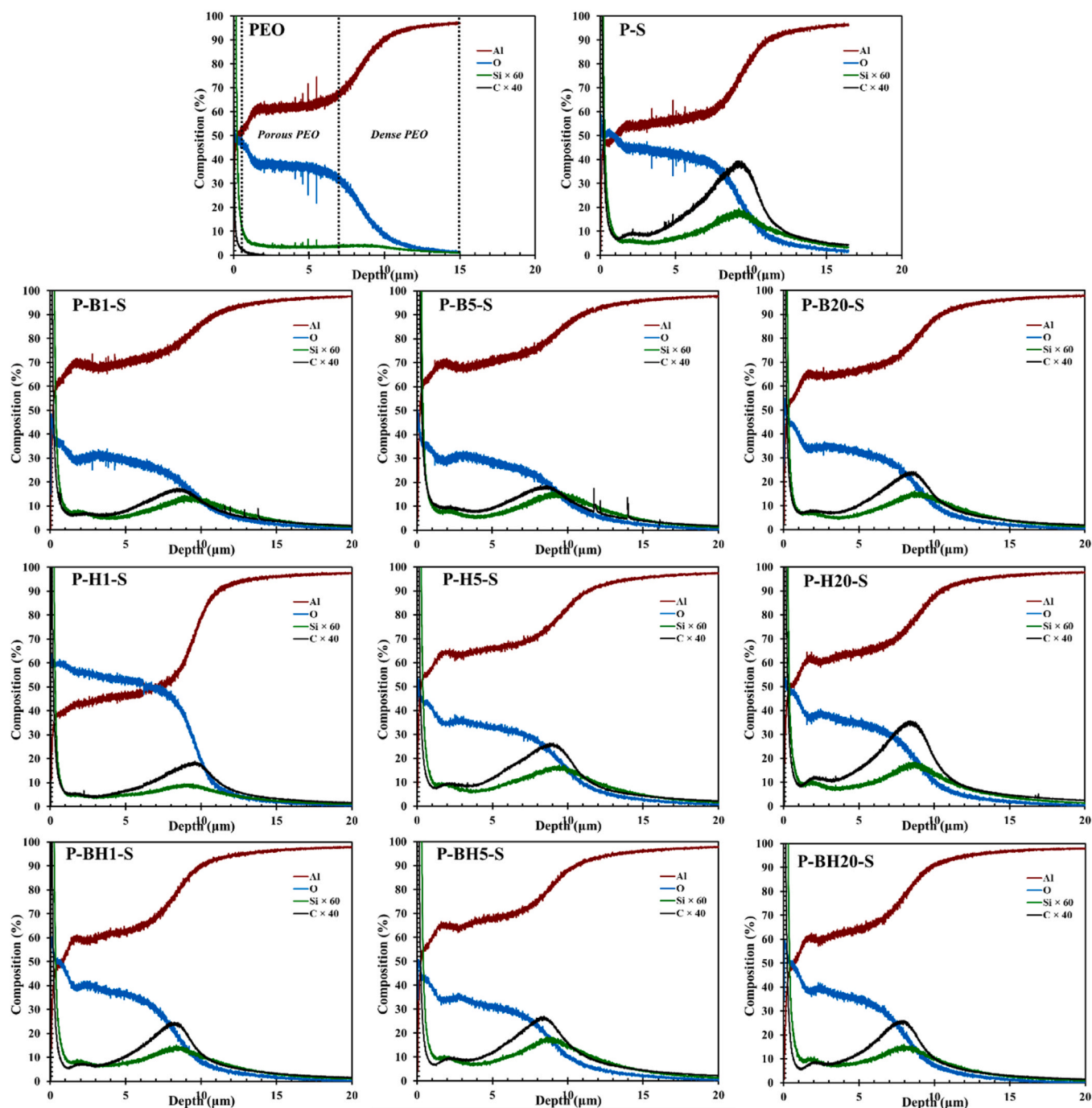
Fig. 8. The elemental depth profiles of different PEO/intermediate/sol-gel coating systems obtained by the GDOES technique. Si and C signals are magnified by 60 and 40 times to facilitate the comparison.

outer layer and inner layer. By application of different types of the intermediate layer, the profile response of C and Si is altered. To get a clearer insight into their role in the sealing ability of the coating system, the area under the curve area of Si and C elements lies in the thickness interval of 1–20 μm was calculated and summarized in Table 2. The C signal of the coating systems in which the BTA was used as the intermediate inhibitive layer is less intense than 8-HQ one in all utilized concentrations. These results are in parallel with the porosity percentage area evaluation of the PEO layer with the intermediate layer prior to the sol-gel application. It is most likely that BTA tends to deposit over the PEO surface whereas 8-HQ is more inclined to diffuse through the pores and cracks. Accordingly, the Si/C ratio of the calculated area was obtained and provided in Table 2. In our previous study [76], it was

confirmed that almost all types of defects could be sealed by the application of this type of sol-gel formulation unless pores and cracks had been filled previously by other types of material. Considering this, in the coating systems, **Eq. 3** was calculated:

The C element inside of the PEO pores irrespective of its presence in the sol-gel structure = .

$$\{[Si/C] \, / \, [Si/C] \, _{P-S}\} \qquad (3)$$

where $[Si/C] \, _{P-S}$ refers to the application of the distinct sol-gel coating on the PEO layer.

Then, the Si element of the sol-gel can be compared with the C element of the inhibitive layer inside of pores regardless of the presence

Table 2
The summarized outcome of the GDOES test of various types of coating systems.

The evaluation of the area (at%.μm) under each curve in the thickness domain of 1–20 μm.

Sample / Element	[C]	[Si]	[Si/C]	{Si/C} / {Si/C} P-S
P-S	244.266	136.444	0.559	1
P-B1-S	139.648	114.372	0.819	1.465
P-B5-S	159.733	138.074	0.864	1.546
P-B20-S	164.738	128.387	0.779	1.393
P-H1-S	143.570	90.305	0.629	1.125
P-H5-S	196.780	151.117	0.768	1.374
P-H20-S	239.894	149.804	0.624	1.116
P-BH1-S	158.042	123.977	0.784	1.402
P-BH5-S	192.676	154.803	0.803	1.437
P-BH20-S	169.201	129.033	0.763	1.365

of C in the sol-gel molecular body. This hypothesis originates from the fact that both sol-gel coating and intermediate layers are organic compounds. On the other hand, the Si element may represent the sol-gel sealing in the coating systems. Hence, mathematical division facilitates the comparison of the sealing ability of the sol-gel coating in the presence of various types of intermediate layers (the higher the value of the division, the higher the sol-gel sealing). Even though the application of the inhibitive layer could result in the decrement of the sol-gel sealing as pores had been filled beforehand, it is worthwhile to mention that chemical attractions of the sol-gel coating with the BTA and 8-HQ inhibitive layers are most likely to happen as documented elsewhere [46]. Interestingly, the values of the division in each group of certain inhibitive materials are maximum when 5 g/l is utilized. To put it another way, the optimum concentration of each inhibitive layer is 5 g/l where maximum sol-gel sealing takes place along with the presence of the inhibitor inside of the PEO pores. Consequently, the sol-gel coating acts as a barrier meanwhile the inhibitive layer operates as a corrosion inhibitor reservoir, as scrutinized in the following section.

3.7. EIS measurements

The electrochemical performance and self-healing properties of different PEO/intermediate/sol-gel coating systems were assessed by EIS test during five weeks of immersion in 0.1 M NaCl solution. The Nyquist and Bode diagrams in which the experimental and fitting data are displayed as markers and solid lines are exhibited in Fig. 9 and 10, respectively. The equivalent electrical circuits (EEC) employed for fitting the EIS outcome are depicted in Fig. 11 and the subsequently fitted output is summarized in Table 3. An outer (porous) layer and an inner (thin) layer are the two main characteristics of the PEO coating [80]. The existence of the porous layer is recognized as a drawback for long-term protection since it creates channels for an aggressive electrolyte to diffuse into the substrate. After 6 h of immersion, EIS fitting of the PEO sample confirmed two-time constants (Fig. 11a) ascribed to the porous layer and dense layer; besides the dominant role of the inner layer for short-term protection as it had a larger resistance [81]. As the time of immersion elapsed, certain PEO layer pores either created or developed, generating routes for the corrosive solution to diffuse [82]. As the coating began to degrade after 24 h, the time constants were modified to take into account the complete coating (porous and inner) as one relaxation process and the substrate response as another. In other words, the EIS data after 24 h turned out to be fitted with EEC in Fig. 11b, revealing how the permeation sequence was split into two stages [83]. In Fig. 11b, R_{ct} and CPE_{dl} stand for the substrate response and R_P and CPE_P stand for the PEO oxide layer. The PEO coating continued to have this electrochemical feature until two weeks of immersion. Afterwards, the one-time constant EEC (Fig. 11c) was employed, bringing out the idea that the protective properties of the PEO coating were broken down, and redox reactions were merely limited by charge transfer resistance [84].

3.7.1. PEO sealed by sol-gel sample

A new time constant that can be detected at high frequencies emerged when the PEO layer was coated with the sol-gel coating. For the P-S, cracks and pores of the PEO layer were sealed by the sol-gel coating which explains using the three-time constant EEC in Fig. 11d. Phase plots could corroborate the presence of the sol-gel over the PEO and the mixed region consisting of the PEO and the sol-gel at high frequencies and middle-range frequencies, respectively. Not only did the R_{SG} appear, but also R_{mix} had greater values than R_p, confirming the pore-filling ability of the sol-gel coating for the porous PEO structure.

For the PEO/intermediate layer/sol-gel coating system, Bode diagrams reported different protection performances in the case of various concentrations and types of the inhibitive layer. Considering the same ratio of inhibitive material and varying concentrations of the impregnation solution, the corrosion resistance properties raised from 1 g/L to 5 g/L, followed by a decrement from 5 g/L to 20 g/L. In other words, the optimum concentration of the inhibitive layer in each group of coating systems seemed to be based on the use of an ethanol solution containing 5 g/L of inhibitor. It might stand to reason that even though the addition of inhibitive species is beneficial to achieve active protective functioning, the mechanical interlocking between the sol-gel layer and the sub-layers plays an important role [85]. As it was shown in the SEM planar images, the higher the concentration of the inhibitive layer, the lower the porosity. Again, even though the outer layer of the PEO layer by itself is a drawback for the long-term protective performance, the porous structure is constructive for the PEO/sol-gel coating system. In another study [86], the beneficial impact of the porous structure of the PEO was confirmed, illustrating that the higher the porosity, the higher the bonding with the sol-gel sealing. In addition to the effect of porosity, the type of inhibitive layer and its inhibition performance are of ultimate importance.

3.7.2. PEO/BTA/Sol-gel samples

Taking BTA into account, brought about deposition over the PEO oxide layer, and correspondingly, the possible chemical interactions between the sol-gel and the deposited BTA layer. In the early stage of the immersion, P-B1-S, P-B5-S, and P-B20-S showed higher resistance to corrosion than P-S which could most likely be thanks to the chemical bonds that occurred between the sol-gel and the intermediate layer. Then, the diffusion of aggressive electrolytes resulted in a decrement in the anti-corrosion performance upon immersion time. In this case, the best protective performance was ascribed to the P-B5-S sample, displaying a sweet spot between mechanical interlocking and chemical interactions.

3.7.3. PEO/8-HQ/Sol-gel cases

For the 8-HQ using the case as an intermediate layer, the pore-filling ability is more dominant than the precipitation over the surface which was confirmed previously in the GDOES and SEM analyses. Moreover, the chemical interaction between the sol-gel and the 8-HQ intermediate layer probably took place which was reported in another investigation [68]. The possible chemical interaction resulted in the enhancement of the corrosion resistance properties of P-H1-S, P-H5-S, and P-H20-S at the initial immersion time as compared to the P-S. Then, the anti-corrosion resistance fell during immersion time. Specifically, for the P-H20-S in which a drastic decrement in protective properties could be found. Considering the diffusion tendency of the 8-HQ through the PEO pores, the significant decrement of the P-H20-S was most likely to the presence of the relatively huge amount of the 8-HQ inside of the pores, having inferior barrier properties than the sol-gel coating. For the 8-HQ intermediate case, the P-H5-S had the best corrosion resistance properties as the optimum amount of the inhibitive species existed along with the sol-gel sealing inside of the pores and cracks.

3.7.4. PEO/BTA+ 8-HQ/Sol-gel samples

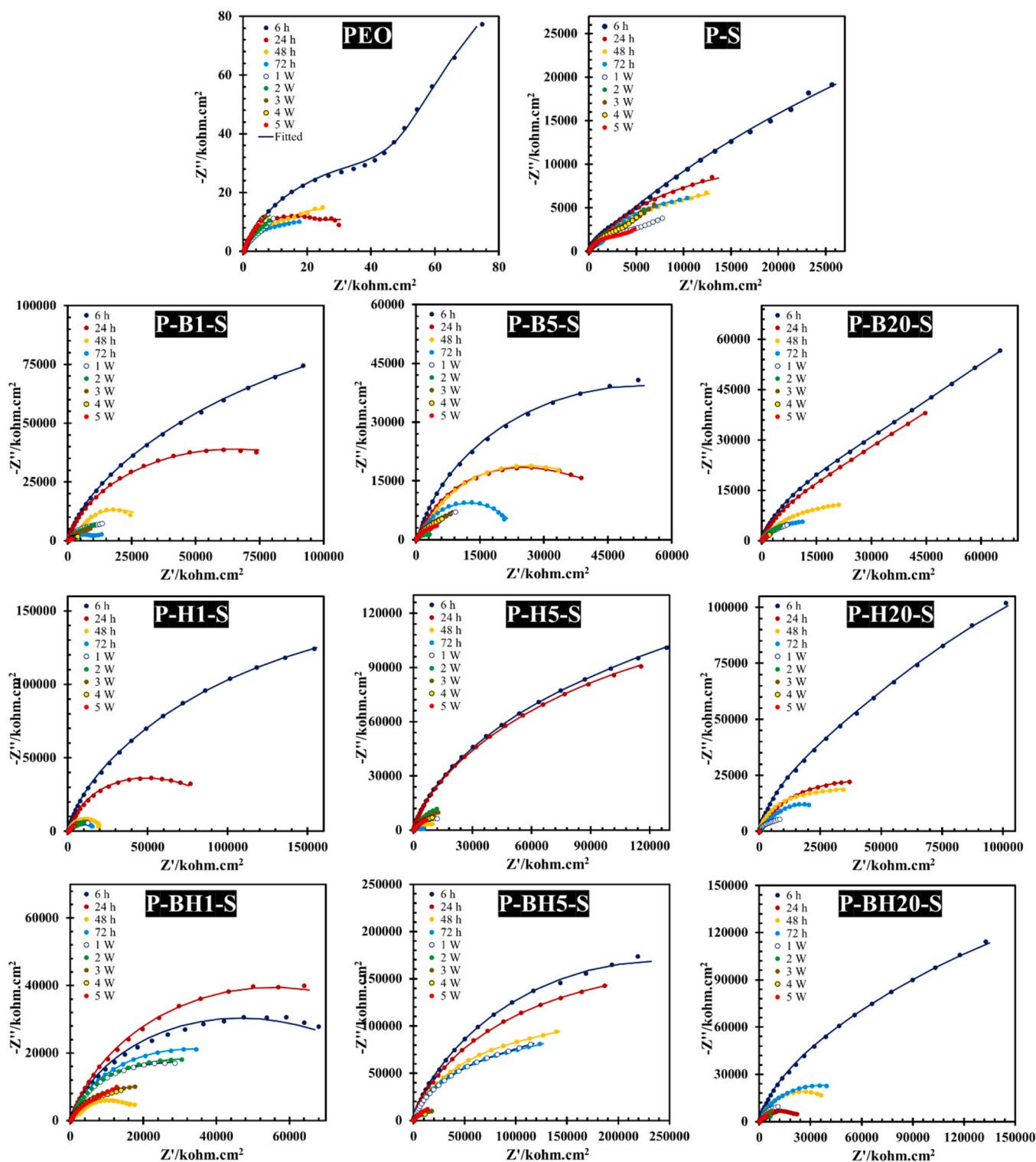In the solution mode of the EIS study, the optimum concentration

Fig. 9. Nyquist plots of various PEO/intermediate layer/sol-gel coating systems during five weeks of immersion in 0.1 M NaCl electrolyte.

ratio of BTA and 8-HQ was revealed (8-HQ/BTA: 7/3) to attain the synergistic inhibition effect in 0.1 M NaCl solution. In this section, the corrosion protection performance of the P-BH-S at different concentrations of the inhibitive layer was examined. By looking at the resistance values obtained by EIS fitting, improvement in the protective performance compared to the systems in which one certain type of inhibitive material was employed could be comprehended at each specific concentration. Particularly, the best corrosion resistance of the whole coating system belonged to the P-BH5-S sample which had a low-

frequency impedance higher than 10^8 Ω cm^2 after two weeks of immersion. Moreover, the time constant at high frequencies was nearly consistent up to one week of immersion, and it exhibited the greatest coating capacitive behavior across the whole frequency range.

To gain a brighter insight through the dual barrier/active properties of the coating systems, the low-frequency impedance was provided in Figs. 12 and 13.

The pore-filling ability of the sol-gel coating caused the enhancement of the low-frequency impedance in the P-S sample which its protective
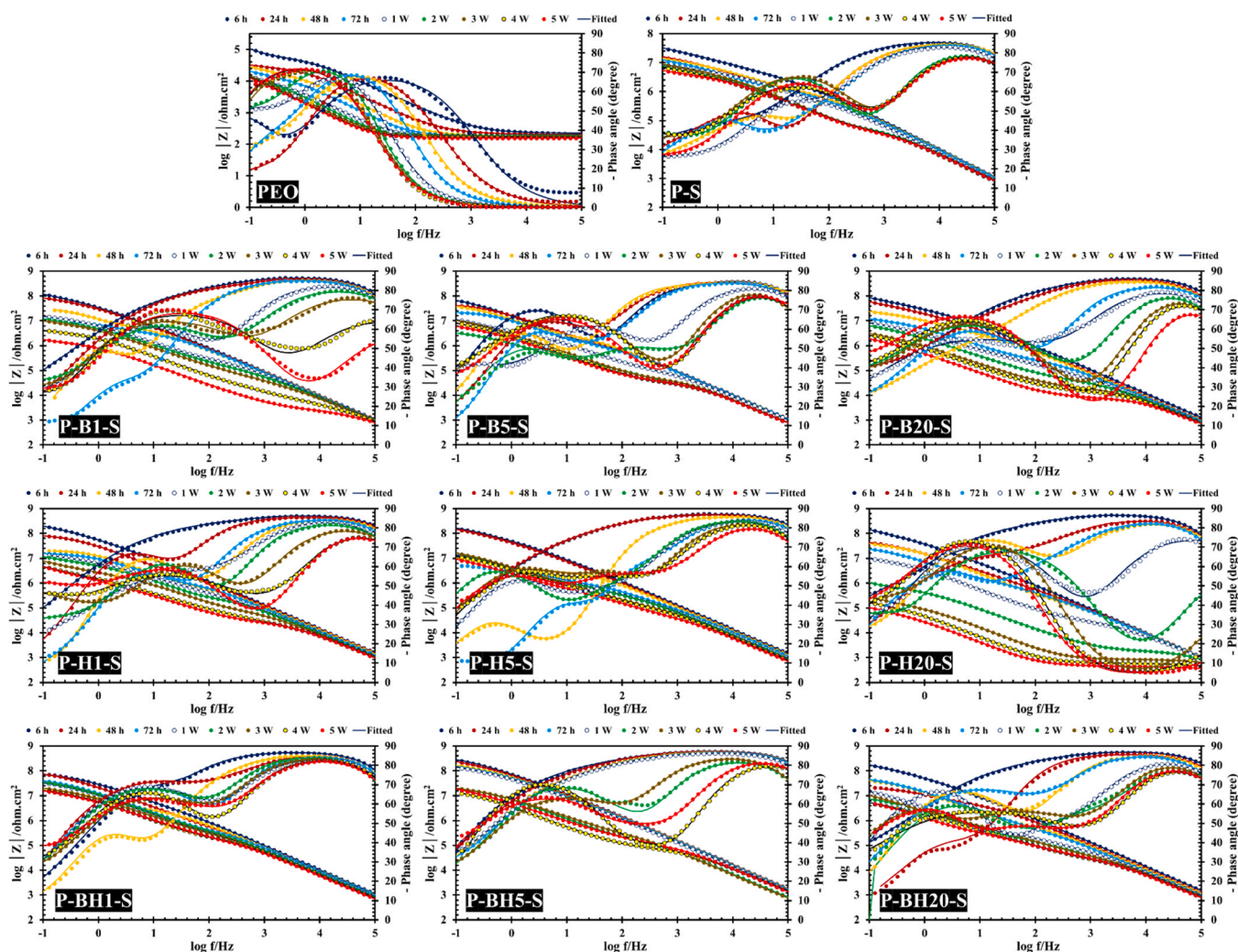
Fig. 10. Bode diagrams of different coating systems during five weeks of exposure to 0.1 M NaCl solution.

features diminished continuously upon immersion. Leaching of inhibitors inducing active protection could be conceived in Fig. 13 with the value of the impedance modulus between two immersion times remaining either constant or heightened. In each group of samples from a certain inhibitive species, the concentration of 5 g/L had the best protective properties, as mechanical interlocking and sufficient sol-gel sealing were presented. For the P-H20-S, insufficient sol-gel sealing caused a significant decrease in corrosion resistance as the release of inhibitors could not compensate for the barrier deficiency. All in all, P-BH5-S had the best corrosion resistance properties after five weeks of exposure to the 0.1 M NaCl electrolyte (modulus at 0.1 Hz: $10^{7.3}$ Ω cm^2). The R_{mix} (RP for the distinct PEO) of the mixed zone consisting of the sol-gel coating, porous PEO layer, and inhibitive layer are also presented in Figs. 12 and 13 to provide a clearer understanding of the protective properties of the coating system. The R_{mix} is considered for the sake of comparison since the distinguishable difference can be detected in this region after corrosion inhibitor doping. Such a notable improvement in mixed-region resistance is reported elsewhere [87]. It might stand to the fact that for the PEO/intermediate/sol-gel coating systems, one time-constant is determined for the mixed region which contained the PEO layer (consisting of the inner dense layer and the outer porous one) along with sol-gel sealing and inhibitive layer. As the thin dense layer is the closest layer to the substrate, any changes in its resistance could be monitored if self-healing action occurred in this zone. In another study, Y. Chen et al. took the R_{mix} and R_{dense} into account separately for Mg alloy which was actively protected by a composite PEO coating that

contains corrosion inhibitors [88]. During a short immersion period, the comparatively weak barrier qualities of the unsealed PEO sample caused an R_P drop, which was then followed by substantial instability, mostly relating to the development of corrosion products. The sealing ability of the sol-gel coating for the porous structure of the PEO could be validated by R_{mix}, whose values are by far higher than R_p. Coating systems having the intermediate layer with 5 g/L concentration provided higher R_{mix} values. At the beginning of immersion, P-H5-S had relatively high R_{mix} values; however, a drastic drop-off in the resistance happened after 72 h immersion. Similarly, for P-H1-S and P-H20-S, it stands to the fact that the presence of 8-HQ mainly inside of the PEO pores occupied the free space for the sol-gel sealing, causing the rapid decrease of R_{mix} and consequently degradation of the coating. For the system having BTA inhibitive layer, the active protection occurs at some specific immersion times. By taking the R_{mix} values after five weeks of immersion for P-B-S and P-H-S in various concentrations, it can be noticed that P-H1-S was more protective than P-B1-S, but contrarily, P-B5-S and P-B20-S had higher corrosion resistance than P-H5-S and P-H20-S, respectively. Although BTA was found inside the PEO pores, the presence of the BTA inhibitive intermediate layer impaired the mechanical interlocking and chemical bonding interplay. The higher concentration of the 8-HQ intermediate, the lower the sol-gel sealing inside of the PEO pores. By comparing the R_{mix} values, P-BH5-S had a superior barrier with active anti-corrosive properties, illustrating the development of active protection by releasing inhibitors, especially after 24 h immersion. The modulus at low frequency illustrated that the corrosion resistance of the
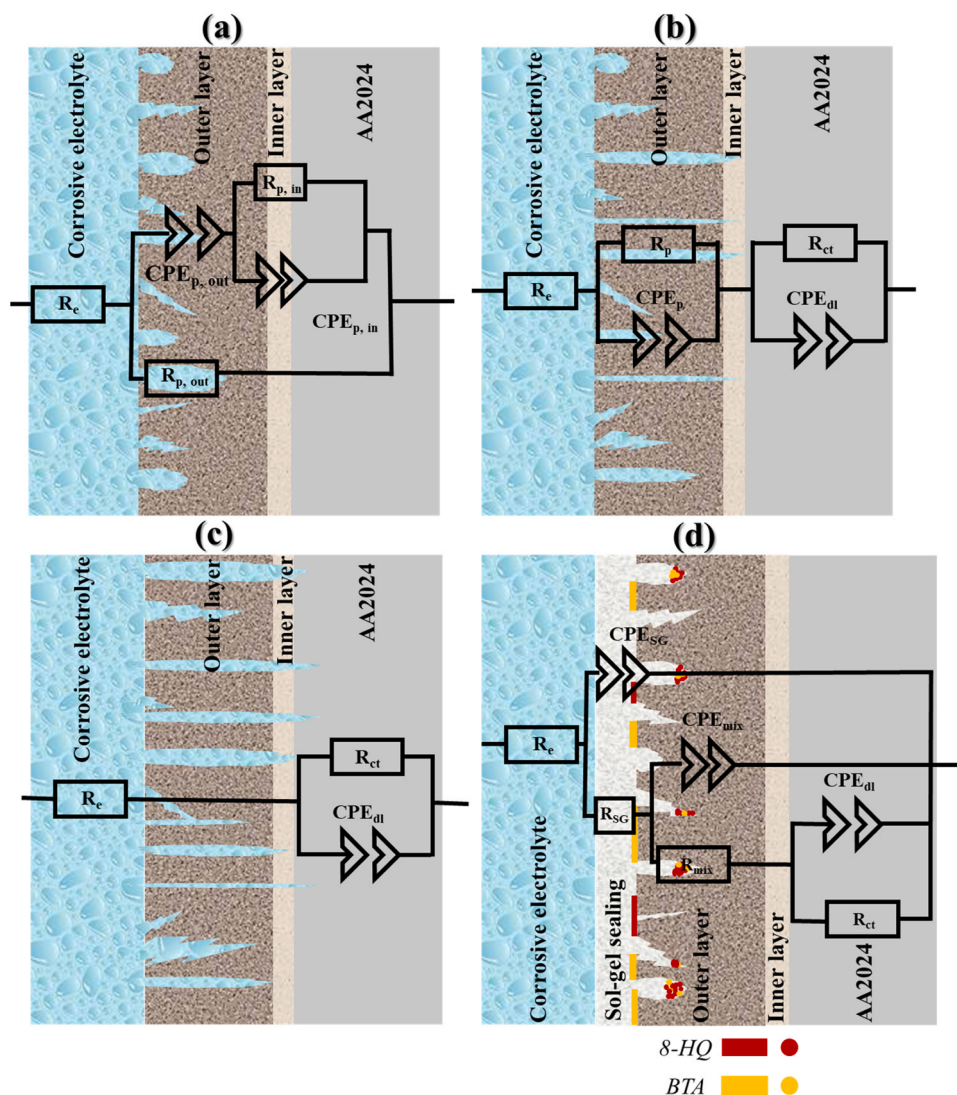
Fig. 11. Different types of the EEC used for the fitting of the EIS output from the different PEO-coated AA2024 systems.

whole system remained almost stable after one week of exposure to the 0.1 M NaCl electrolyte; meanwhile, R_{mix} values are along with ups and downs. Meaning that, apart from the sol-gel sealing as the barrier, releasing the inhibitors in the mixed region kept the corrosion resistance properties almost consistent in the P-BH5-S sample. Interestingly, its self-healing remained functioning even after 5 weeks of exposure to the 0.1 M NaCl solution.

The effective capacitance of the PEO-coated samples was evaluated by Eq. 4 [59] depicted in Figs. 12 and 13.

$$C_{mix} = Y_{0, mix}^{1/n} R_{mix}^{(1-n)/n} \tag{4}$$

According to the formula $C = \varepsilon\varepsilon_0 A/d$, capacitance is inversely proportional to the thickness of the coating, and water diffusion increases coating permittivity resulting in the elevating coating capacitance. Facile diffusion routes of the electrolyte through the unsealed PEO layer caused a significant increase in the capacitance after a short period of immersion. A notable decrease was observed in the unsealed PEO sample after the application of the sol-gel coating. As the thickness of the mixed region fluctuates in the order of micrometers, low capacitance values might be anticipated. For the P-S sample in which all pores were merely filled by the sol-gel sealing, an almost increasing trend of the effective capacitance was observed. After the application of the intermediate layers, the effective capacitance of the mixed region had

different tendencies. Regardless of the type of the intermediate layer, the ones with 20 g/L had relatively higher capacitance values during immersion times, illustrating the lower barrier properties. Particularly in the P-H20-S sample, in which the 8-HQ existed mostly inside of the pores, a drastic enhancement of the effective capacitance in the mixed region was observed. In the coating systems having a 5 g/L inhibitive layer, on the one hand, the sol-gel sealing acts as an obstacle against the electrolyte diffusion, and on the other hand, leaches the corrosion inhibitors; thus, obtaining the minimum effective capacitance compared to other concentrations in the mixed region. Accordingly, the lowest effective capacitance was attributed to the P-BH5-S sample, having the synergistic corrosion inhibition characteristic along with adequate sol-gel sealing. Thus, the optimum of the involved influential parameters was found when both 8-HQ and BTA with the respective ratio of 7–3 presented at 5 g/L concentration which is why P-BH5-S had the highest dual protective performance.

3.8. SVET

The dual active/passive performance of the coated samples was electrochemically examined by SVET testing conducted in 15 mM NaCl solution, as exhibited in Fig. 14. The cut-edge configuration in which the exposed area of the coated samples is ± 2.3 mm² was employed to attain the SVET outcome up to 12 h immersion. In this mode, the aggressive

Table 3

The obtained electrochemical parameters of PEO/intermediate/sol-gel coating systems after five weeks of immersion in 0.1 M NaCl electrolyte.

Sample	Immersion time in an hour (h) and week (w)	R_{SG} (kΩ cm^2)	CPE_{SG}		R_{mix} or RP (kΩ cm^2)	CPE_{mix} or CPE_p		R_{ct} (kΩ cm^2)	CPE_{dl}	
			Y_0 (nΩ^{-1} cm^{-2} s^n)	n		Y_0 (nΩ^{-1} cm^{-2} s^n)	n		Y_0 (nΩ^{-1} cm^{-2} s^n)	n
PEO	6 h	-	-	-	75	3593	0.79	293	16,051	0.96
	24 h	-	-	-	36	72,787	0.64	20	8757	0.91
	48 h	-	-	-	37	49,143	0.79	10	21,241	0.90
	72 h	-	-	-	23	64,442	0.89	7	33,149	0.92
	1w	-	-	-	41	119,420	0.91	5	66,165	0.90
	2w	-	-	-	32	149,470	0.97	6	86,905	0.91
	3w	-	-	-	-	-	-	38.15	85,187	0.87
	4w	-	-	-	-	-	-	38.18	98,024	0.88
	5w	-	-	-	-	-	-	38.03	103,210	0.88
P-S	6 h	679.29	2.18	0.96	36,584	31.16	0.44	153,600	2.90	0.82
	24 h	312.65	2.43	0.96	2912	56.91	0.43	34,614	4.02	0.97
	48 h	294.10	2.52	0.95	2313	51.11	0.44	45,228	9.33	0.94
	72 h	276.12	2.53	0.96	4088	55.39	0.51	20,966	15.57	0.93
	1w	448.51	3.87	0.94	4412	22.75	0.74	25,744	198.94	0.52
	2w	59.61	5.04	0.92	4021	32.62	0.84	23,820	200.65	0.70
	3w	47.59	4.72	0.93	5308.40	34.02	0.81	21,820	171.22	0.69
	4w	47.41	5.13	0.93	5089.60	55.88	0.75	37,240	237.39	0.67
	5w	50.88	6.13	0.91	2895.10	39.96	0.80	32,948	330.58	0.45
P-B1-S	6 h	2378.70	2.26	0.97	146,200.0	5.21	0.58	206,500	8.35	0.56
	24 h	2016.90	2.46	0.96	8523.3	1.64	0.76	142,000	6.74	0.46
	48 h	1160.50	2.65	0.96	7104.4	5.58	0.70	28,106	13.34	0.91
	72 h	1900.40	2.84	0.96	2313.9	8.90	0.69	5933	27.57	0.82
	1w	271.93	3.80	0.94	15,494.0	28.03	0.75	32,129	221.00	0.70
	2w	150.66	5.20	0.91	11,894.0	36.35	0.73	32,575	191.14	0.74
	3w	68.76	8.59	0.87	11,491.0	42.80	0.73	13,239	379.02	0.92
	4w	12.92	38.47	0.77	4495.9	61.63	0.80	3662	1145.60	0.97
	5w	3.27	43.50	0.76	1660.4	171.75	0.81	1999	1796.70	0.89
P-B5-S	6 h	1283.50	2.66	0.95	78,791	9.50	0.86	28,682	58.21	0.94
	24 h	1779.80	2.89	0.95	46,072	9.18	0.80	48,510	314.87	0.93
	48 h	2804.10	3.27	0.94	46,256	15.74	0.83	52,781	494.15	0.92
	72 h	926.61	2.86	0.95	3193.2	10.99	0.80	20,114	5.51	0.92
	1w	130.31	3.62	0.94	3857.9	23.53	0.79	41,980	108.11	0.63
	2w	26.61	4.26	0.95	412.1	88.05	0.71	3798	1150.7	0.77
	3w	47.03	4.53	0.94	2718.0	58.47	0.81	43,043	67.34	0.32
	4w	34.24	4.87	0.94	7097.1	79.13	0.80	37,140	181.84	0.53
	5w	38.36	6.29	0.92	6991.7	101.62	0.79	34,050	482.63	0.70
P-B20-S	6 h	1874.00	1.93	0.97	78,137.0	6.97	0.55	532,400	10.57	0.58
	24 h	1735.10	2.73	0.96	40,914.0	8.93	0.61	344,000	17.10	0.54
	48 h	1091.3	3.16	0.95	36,952.0	26.88	0.54	288,500	238.39	0.60
	72 h	273.50	4.31	0.93	10,808.0	36.88	0.76	118,400	236.58	0.40
	1w	97.76	6.29	0.91	16815.0	96.16	0.62	72,330	1105.00	0.88
	2w	41.47	6.23	0.92	9716.2	114.44	0.74	13,892	384.80	0.89
	3w	19.05	6.65	0.92	4195.1	223.52	0.76	5989	811.24	0.90
	4w	14.74	7.66	0.91	3479.6	280.08	0.78	4244	757.10	0.90
	5w	7.98	9.33	0.89	2996.2	451.13	0.79	4398	958.27	0.91
P-H1-S	6 h	2961.30	1.59	0.97	65741.0	2.32	0.61	710,900	2.73	0.32
	24 h	4226.70	1.96	0.95	78748.0	4.11	0.85	19,887	67.69	0.88
	48 h	638.44	2.12	0.95	1386.5	8.04	0.83	19,398	2.36	0.94
	72 h	198.56	2.09	0.96	1180.2	8.71	0.58	16,265	9.28	0.85
	1w	258.79	2.83	0.95	16767.0	36.51	0.62	16,590	232.84	0.63
	2w	273.40	3.70	0.93	4492.5	17.35	0.86	64,823	123.46	0.50
	3w	86.77	4.95	0.91	2513.9	31.20	0.80	77,510	165.24	0.64
	4w	26.63	5.80	0.90	4988.8	157.07	0.66	16,772	210.97	0.85
	5w	26.83	6.01	0.90	3287.6	150.52	0.73	12,481	179.29	0.89
P-H5-S	6 h	4109.00	1.55	0.97	368,400.0	4.45	0.53	146,900	23.27	0.89
	24 h	3981.90	1.83	0.97	360,800.0	5.10	0.53	135,700	40.94	0.89
	48 h	735.78	1.91	0.97	2317.7	7.72	0.58	9657	88.37	0.81
	72 h	266.88	2.28	0.96	778.9	4.96	0.86	2597	28.89	0.83
	1w	280.46	3.24	0.95	2019.2	35.78	0.69	17,963	22.53	0.85
	2w	302.26	3.45	0.95	1296.2	25.47	0.74	36,773	43.46	0.82
	3w	152.47	4.10	0.95	1113.3	18.10	0.84	28,228	38.06	0.70
	4w	95.69	4.00	0.95	2743.0	58.22	0.68	19,673	14.91	0.84
	5w	47.80	4.34	0.95	1919.0	77.07	0.66	17,543	32.10	0.84
P-H20-S	6 h	4130.7	2.24	0.97	139,900.0	3.80	0.61	302,000	6.07	0.77
	24 h	739.34	3.08	0.95	64,765	13.30	0.65	71,850	173.16	0.90
	48 h	344.64	3.61	0.93	34,595	7.24	0.85	41,907	73.29	0.76
	72 h	298.05	3.27	0.94	2480.9	22.16	0.65	34,461	9.39	0.87
	1w	37.70	9.71	0.86	10,327	45.77	0.83	10,355	351.80	0.92
	2w	1.96	20.95	0.80	815.01	362.11	0.81	1386	1944.90	0.91
	3w	0.95	29.47	0.73	143.08	1567.00	0.88	744	4679.90	0.68
	4w	0.55	268.13	0.60	178.05	3723.00	0.88	172	14,385.00	0.98
	5w	0.42	2027.30	0.46	137.73	6001.6	0.88	123	17,032.00	0.97

Table 3 (*continued*)

Sample	Immersion time in an hour (h) and week (w)	R_{SG} (kΩ cm²)	CPE_{SG}		R_{mix} or RP (kΩ cm²)	CPE_{mix} or CPE_p		R_{ct} (kΩ cm²)	CPE_{dl}	
			Y_0 (nΩ⁻¹ cm⁻² sⁿ)	n		Y_0 (nΩ⁻¹ cm⁻² sⁿ)	n		Y_0 (nΩ⁻¹ cm⁻² sⁿ)	n
P-BH1-S	6 h	2575.7	2.09	0.97	6223.6	6.31	0.52	96,294	0.87	0.92
	24 h	487.08	2.50	0.97	4698.2	7.43	0.70	109,200	0.65	0.93
	48 h	1072.60	2.76	0.96	3187.1	12.81	0.60	15,418	15.92	0.90
	72 h	480.38	2.77	0.96	4394.2	11.12	0.83	108,800	13.88	0.25
	1w	345.30	3.65	0.95	39,490	15.39	0.79	22,780	153.68	0.84
	2w	517.87	3.67	0.96	39,865	13.98	0.78	26,423	115.95	0.76
	3w	325.40	4.02	0.95	23,098	25.05	0.73	28,299	191.45	0.68
	4w	224.48	4.66	0.94	15,938	28.23	0.81	21,277	161.91	0.76
	5w	187.44	4.93	0.94	20,617	36.68	0.73	32,366	167.59	0.92
P-BH5-S	6 h	7350.30	1.23	0.98	355,700	1.98	0.60	158,600	1.72	0.92
	24 h	6543.40	1.31	0.97	472,300	2.77	0.56	98,059	35.75	0.94
	48 h	5559.80	1.38	0.97	270,700	3.39	0.57	96,770	29.36	0.95
	72 h	3829.60	1.44	0.97	229,600	3.70	0.57	95,330	28.33	0.94
	1w	3228.00	1.63	0.97	240,300	4.24	0.56	93,330	27.47	0.96
	2w	185.60	4.34	0.94	20,740	22.52	0.81	10,187	185.76	0.94
	3w	325.40	4.02	0.95	23,098	25.05	0.73	28,299	191.45	0.68
	4w	65.45	2.91	0.93	19,032	36.50	0.82	17,761	16.49	0.90
	5w	89.02	2.27	0.95	37,951	44.60	0.70	36,649	3.98	0.94
P-BH20-S	6 h	3432.40	1.51	0.97	251,100	3.64	0.56	267,800	6.17	0.75
	24 h	3834.90	2.20	0.96	20,264	22.71	0.69	41,582	8657.50	0.42
	48 h	767.54	2.49	0.95	48,592	12.42	0.81	25,980	589.63	0.92
	72 h	496.83	2.70	0.96	58,573	12.62	0.74	12,069	135.18	0.93
	1w	84.33	3.55	0.95	530.00	45.30	0.70	27,394	20.71	0.97
	2w	38.15	4.71	0.94	302.88	50.99	0.69	10,530	44.14	0.81
	3w	40.12	3.52	0.95	2986.80	81.00	0.67	22,582	29.20	0.91
	4w	26.05	4.42	0.94	10,469	158.98	0.64	7484	936.73	0.84
	5w	30.20	4.87	0.94	1046.90	168.90	0.63	14,135	35.79	0.97

electrolyte could reach the lateral regions of the AA2024 substrate through preferred pores, cracks, and any other defects of the PEO coating, leading to the creation of differential aeration cells. In other words, one could expect that the typical crevice corrosion might happen at the borders in this corrosion evaluation set-up [89]. Furthermore, due to the poor resistive qualities of the passive layer over the S-phase, which expose the substrate to an aggressive environment, AA2024 is vulnerable to localized corrosion [90]. So, both crevice and localized corrosion processes occur in the hidden surfaces, but most importantly, in the scanned surface. For the PEO sample, some intense anodic activities are found to be at the border and somehow in the middle of the exposure area, referring to the crevice corrosion and pitting corrosion, respectively. It can be comprehended, the anodic activities and coating deterioration enhanced from 3 h to 12 h immersion time as the cross-section configuration greatly facilitates the access of aggressive elements to the substrate. Upon the use of a sol-gel coating, pores and defects which might have induced local corrosion phenomenon at the borders were sealed, which is why the decrement of anodic activity at the borders is recognized in the P-S sample. While the local pitting corrosion took place at the scanning area, enhancing with immersion time. For the system having an inhibitive intermediate layer, it is noteworthy to mention that pores were filled either by the sol-gel or the inhibitive compounds. Accordingly, the barrier performance of the pores filled with the inhibitive layer is not as much as the ones sealed with the distinct sol-gel layer, therefore, local corrosion phenomenon is possible to happen at the borders. Then the self-healing properties of the corrosion inhibitor define the protective performance upon immersion time. After the application of benzotriazole as an intermediate layer for the PEO/sol-gel coating system, local anodic activity appeared at the vertical border. The inhibitor leaching brought about the decrement of the anodic activity at 6 h of immersion; however, it seems that its protective functioning was not persistent to last any longer. More severe anodic activity occurred in the P-B5-S sample after 12 h immersion. This outcome is quite in accordance with other characterization analyses (GDOES and SEM), revealing the presence of benzotriazole mostly over the PEO surface. The lack of the inhibitive species might be a reason for the poor self-healing functioning of the P-B5-S sample in the cut-edge

configuration. For the P-H5-S sample, no trace of the anodic activity can be found at the borders after 3 h of immersion, while the pitting corrosion of the substrate happened in the middle regions. The local anodic activity has been significantly reduced in the P-H5-S as compared to the P-B5-S sample. In parallel to the SEM section, the tendency of hydroxyquinoline is relatively higher than benzotriazole to penetrate the PEO pores, leading to the creation of pores filled with inhibitors. Accordingly, it can be understood that there was an interplay between the inhibitors release on the one hand and penetration of Cl⁻ containing electrolytes on the other hand. Even though the optical microscopic image does not exhibit the corrosion attack, the SVET maps report an ongoing anodic activity that is not as intense as the one in the P-B5-S sample. Interestingly for the P-BH5-S, both inhibitors act with certain affinities to either diffuse or deposit. In the beginning (after 3 h), intense anodic activity can be detected in the middle regions, which is attributed to the localized corrosion of the substrate. Releasing of the inhibitors could dramatically diminish the anodic activity in the central regions after 6 h, meanwhile, the anodic activity at the border becomes more noticeable. The promising protective properties of the inhibitors lead to the complete protection of the exposed area after 12 h immersion in which no sign of anodic activity could be perceived. The optical image after 12 h immersion confirmed that the P-BH5-S illustrated the best protective performance which is in parallel with the EIS analysis.

3.9. Corrosion protection mechanism

A schematic representation of different coating systems is provided in Fig. 15. The promising sealing and pore-filling properties of the sol-gel coating for the PEO layer are depicted for the P-S sample. Utilizing BTA as the intermediate layer (P-B-S) led to the deposition over the PEO surface dominantly as well as partial diffusion through the pores. Although chemical interactions may happen between the intermediate layer and the sol-gel sealing, mechanical interlocking is also of great importance. Varying the concentration of BTA may result in obtaining a different number of chemical and physical bonds in which the concentration of 5 g/L was the optimum. Having 8-HQ as the intermediate layer showed more inclination to be diffused into the pores than
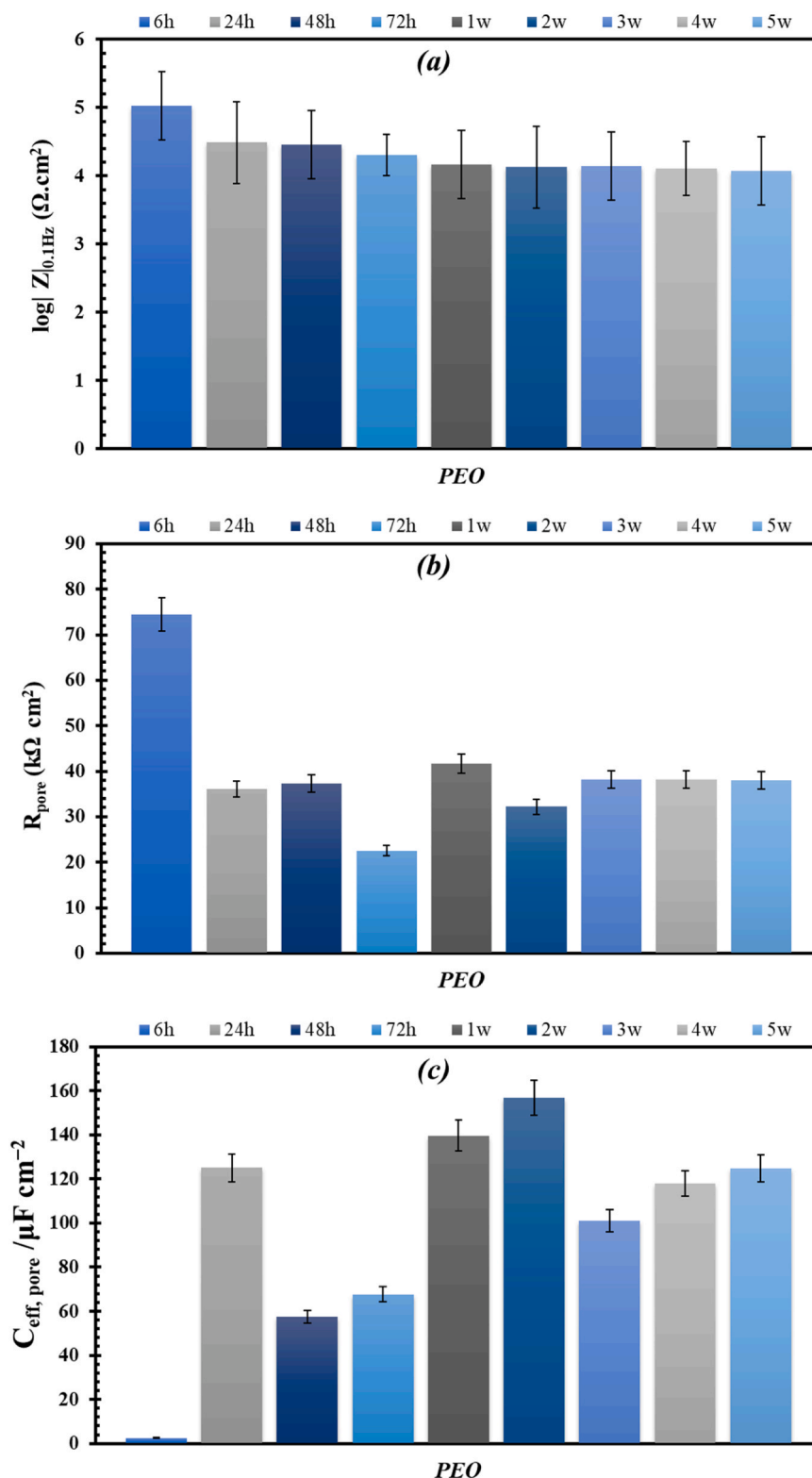
Fig. 12. The evolution of the low-frequency impedance (a), pore resistance (b), and effective capacitance (c) of the PEO sample upon five weeks of exposure to the simulated corrosive electrolyte.

precipitation over the PEO oxide layer. Hence, the more the concentration of the 8-HQ intermediate layer, the more presence of the 8-HQ inside of PEO pores. GIXRD and EDS analyses confirmed the presence of copper oxide over the PEO surface. Besides, as it is well-documented [47,71,72,91,92] the corrosion inhibition of the BTA mainly acts on Cu-rich intermetallic particles and cupper oxides. Hence, BTA tends to

precipitate over the PEO surface rather than diffuse into the pores. On the other hand, BTA has a molecular weight of approximately 119 g/mol, while HQ has a molecular weight of around 145 g/mol. According to their molecular weights, it can be concluded that BTA is smaller in size than 8-HQ. As BTA is smaller than 8-HQ, it has a higher diffusion coefficient and a higher tendency for diffusion. Therefore, one
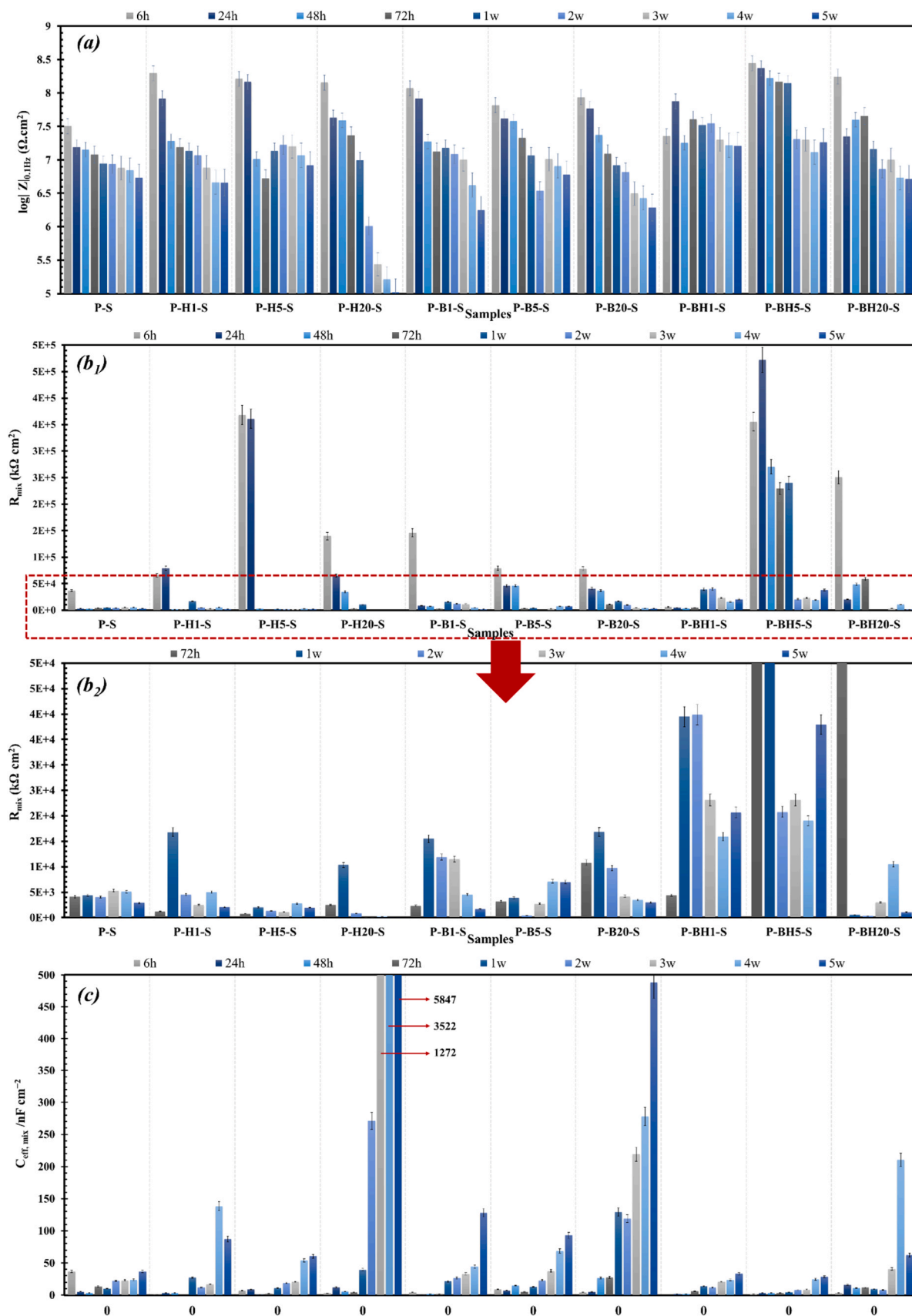
Fig. 13. The advancement of the EIS modulus at low-frequency (a), the mixed-region resistance (b₁) and its magnified version of the relevant region (b₂), and the mixed-region capacitance (c) of the coating system during five weeks of exposure to 0.1 M NaCl solution. The numbers 1272, 3522, and 5847 in (c) refer to the effective capacitance of P-H20-S after 3, 4, and 5 weeks.
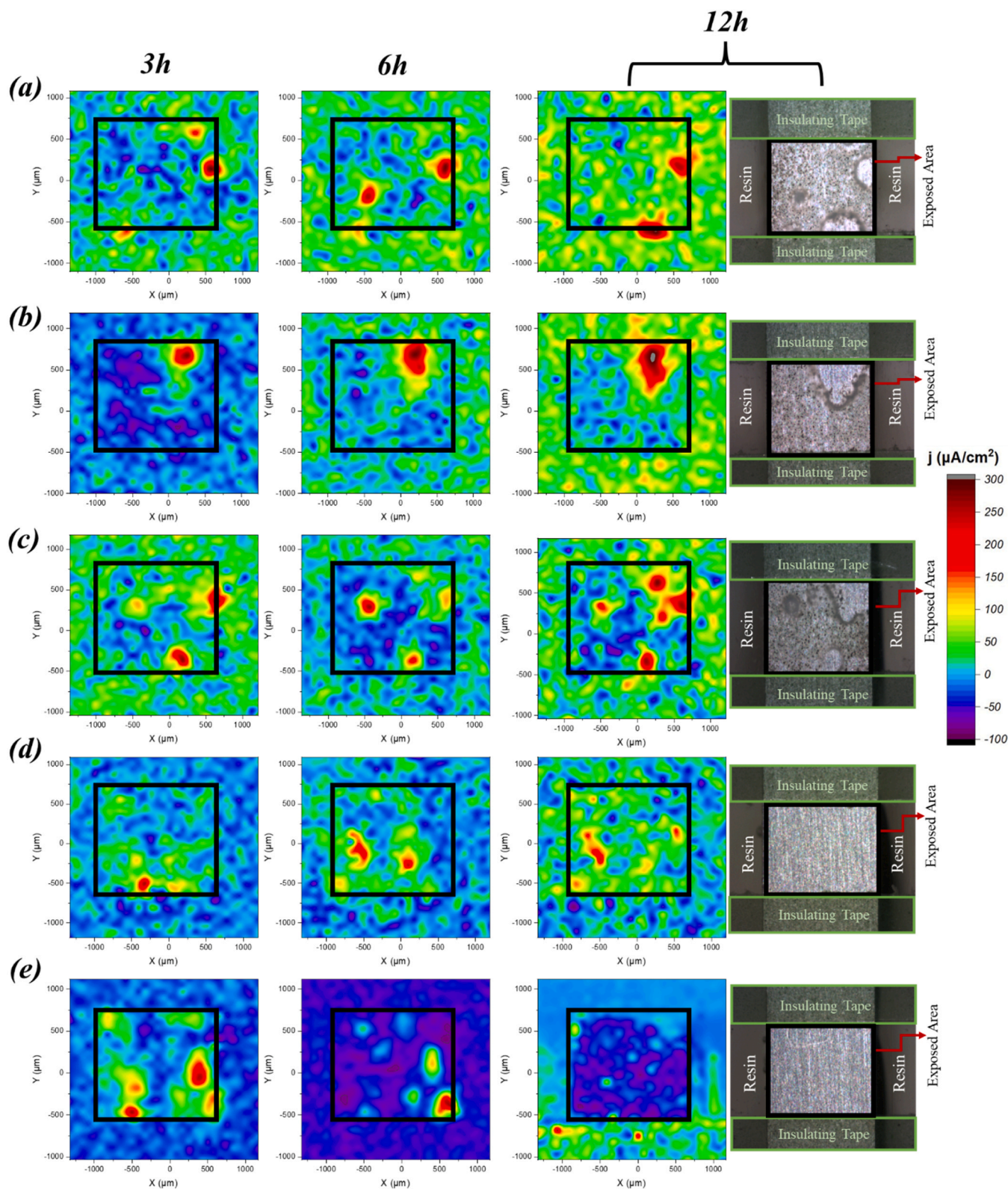
Fig. 14. SVET maps of the PEO (a), P-S (b), P-B5-S (c), P-H5-S (d), and P-BH5-S (e) samples after 3 h, 6 h, and 12 h immersion in 15 mM NaCl solution as well as the optical image at the end of the test.

could have expected that BTA could penetrate through the PEO pores more than 8-HQ. Controversially in our study, it was noticed that BTA tends to precipitate over the PEO surface while 8-HQ favors diffuse through the PEO pores. The interactions between BTA and the PEO surface or particularly the copper oxide may be responsible for this behavior, leading to the preferential adsorption or deposition of BTA on the PEO surface. All in all, this outcome indicated the complex relation between diffusion, molecular size, and surface interactions in determining the behavior of corrosion inhibitors within the coating system. When the sol-gel coating is applied to the PEO-loaded inhibitors, it does
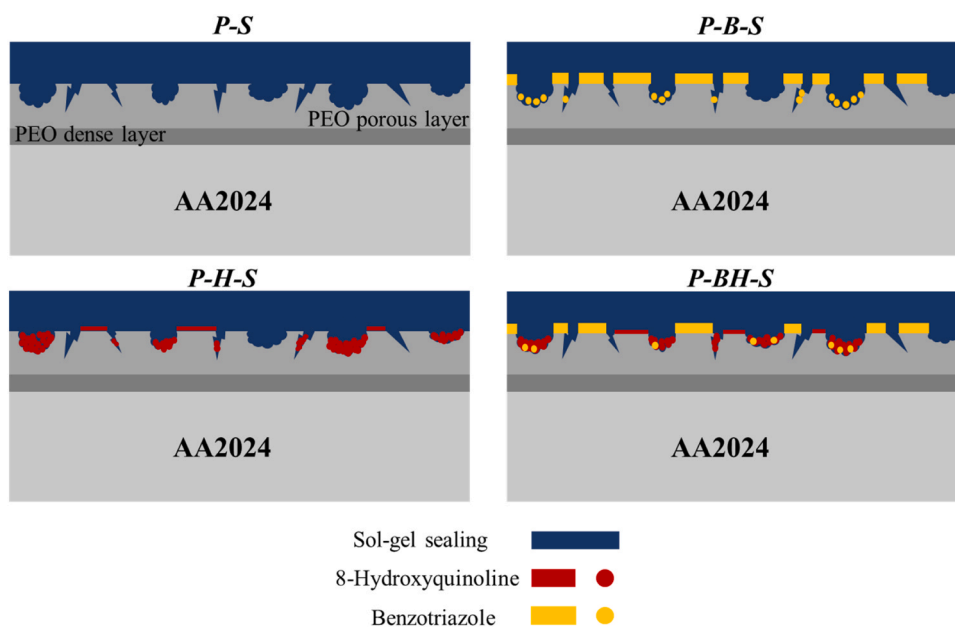
Fig. 15. The schematic illustration of various sealing (sol-gel doped with inhibitive species) coating systems for the PEO layer on AA2024.

not have free space to seal as it is already occupied by 8-HQ intermediate layer. Consequently, one could believe that apart from having possible chemical bonds between 8-HQ and the sol-gel, the higher concentration of the 8-HQ intermediate layer may decrease the barrier properties. S. Marcelin and N. P é bère [75] stated that the combination of BTA and 8-HQ had a synergistic impact on the corrosion resistance of an AA2024 alloy in a way that BTA affects mostly Cu-rich intermetallic particles while the 8-HQ mainly acts on the Al matrix, due to its chelating effect. They also reported a substantial decrease in the galvanic coupling which is the main reason for the corrosion process of AA2024 when both corrosion inhibitors (BTA and 8-HQ) are presented simultaneously. D. Fix et al. [93] investigated the corrosion resistance properties of a sol-gel coating modified with 8-HQ and BTA-loaded halloysite nanotubes on an AA2024 substrate. They showed that the corrosion inhibition mechanism is owing to the construction of complexes between the released corrosion inhibitors and the substrate which makes a physical barrier. In the P-BH-S coating system and more specifically at the mixed region, some hypotheses could be made to explain the superior protective properties: 1) BTA species on top of the PEO layer could generate more chemical bonds with the sol-gel apart from its inhibition performance; 2) the 8-HQ mainly present inside the porosity, makes the pores operating as inhibitor reservoirs; and 3) The synergistic effect between BTA and 8-HQ could generate reliable self-healing properties to the whole system as it was also corroborated in other works [75,93]. The three mentioned criteria together with the mechanical interlocking between the sol-gel and the sub-layer was maximized in the P-BH5-S, making it the best coating system.

4. Conclusion

The self-healing properties were induced in PEO coating by layer-by-layer fabrication of the corrosion inhibitor layer along with sol-gel sealing. The concentration of the intermediate layer plays a crucial role as it affects not only the mechanical interlocking and chemical bindings with the sol-gel layer but also the barrier properties. The following conclusions can be made:

I. The synergistic inhibitive behavior in the 0.1 M NaCl solution was found between 8-hydroxyquinoline and benzotriazole with a ratio of 7/3, respectively.

II. The PEO porosity can be considered natural 'cages' for surface impregnation/sealing (the higher the concentration of the inhibitive layer, the lower the porosity).

III. The optimum concentration of the ethanolic solution used to form the inhibitive layer was 5 g/L, providing both mechanical interlocking and self-healing properties in the PEO/intermediate/sol-gel coating system.

IV. The highest corrosion protection performance was related to P-BH5-S, revealing reliable results after five weeks of immersion in the neutral chloride solution.

CRediT authorship contribution statement

Sajjad Akbarzadeh: Investigation, Methodology, Validation, Writing- Original draft preparation, Writing - review & editing. **Leonardo Bertolucci Coelho**: Methodology, Validation. **Lisa Dangreau**: Investigation, Validation. **Alex Lanzutti**: Investigation, Validation; **Lorenzo Fedrizzi**: Investigation, Validation. **Marie-Georges Olivier**: Conceptualization, Methodology, Validation, Writing - review & editing, Supervision, Funding acquisition.

Declaration of Competing Interest

The authors declare that they have no known competing financial interests or personal relationships that could have appeared to influence the work reported in this paper.

Data availability

Data will be made available on request.

Acknowledgments

References

[1] V. Jothi, A.Y. Adesina, A. Madhan Kumar, J.S. Nirmal Ram, Influence of organic acids on the surface and corrosion resistant behavior of anodized films on aa2024 aerospace alloys in artificial seawater, Met. Mater. Int. 26 (2020) 1611–1620.

[2] X. Zhang, X. Zhou, T. Hashimoto, B. Liu, Localized corrosion in AA2024-T351 aluminium alloy: Transition from intergranular corrosion to crystallographic pitting, Mater. Charact. 130 (2017) 230–236.

[3] N. Murer, R. Oltra, B. Vuillemin, O. Néel, Numerical modelling of the galvanic coupling in aluminium alloys: A discussion on the application of local probe techniques, Corros. Sci. 52 (2010) 130–139.

[4] M.B. Vukmirovic, N. Dimitrov, K. Sieradzki, Dealloying and corrosion of Al alloy 2024-T3, J. Electrochem. Soc. 149 (2002) B428.

[5] K.A. Yasakau, J. Tedim, M.L. Zheludkevich, M.G.S. Ferreira, Smart self-healing coatings for corrosion protection of aluminium alloys, Handb. Smart Coat. Mater. Prot. (2014) 224–274.

[6] V.R. Capelossi, M. Poelman, I. Recloux, R.P.B. Hernandez, H.G. De Melo, M. G. Olivier, Corrosion protection of clad 2024 aluminum alloy anodized in tartaric-sulfuric acid bath and protected with hybrid sol–gel coating, Electrochim. Acta 124 (2014) 69–79.

[7] A.I. Ryabchikov, E.B. Kashkarov, A.E. Shevelev, A. Obrosov, D.O. Sivin, Surface modification of Al by high-intensity low-energy Ti-ion implantation: Microstructure, mechanical and tribological properties, Surf. Coat. Technol. 372 (2019) 1–8.

[8] L.F. Wang, J. Sun, X.L. Yu, Y. Shi, X.G. Zhu, L.Y. Cheng, H.H. Liang, B. Yan, L. J. Guo, Enhancement in mechanical properties of selectively laser-melted AlSi10Mg aluminum alloys by T6-like heat treatment, Mater. Sci. Eng. A 734 (2018) 299–310.

[9] C. Haixiang, K. Dejun, Comparison on electrochemical corrosion performances of arc and laser thermal sprayed Al–Ti–Ni coatings in marine environment, Mater. Chem. Phys. 251 (2020) 123200.

[10] G.M. Rao, Dilkush, A.V. Gopal, Effect of physical vapour deposition coated and uncoated carbide tools in turning aluminium alloy-AA6063, Mater. Today Proc. 41 (2021) 1212–1219.

[11] F. Yu, L. Camilli, T. Wang, D.M.A. Mackenzie, M. Curioni, R. Akid, P. Bøggild, Complete long-term corrosion protection with chemical vapor deposited graphene, Carbon N. Y 132 (2018) 78–84.

[12] X. Verdalet-Guardiola, B. Fori, J.P. Bonino, S. Duluard, C. Blanc, Nucleation and growth mechanisms of trivalent chromium conversion coatings on 2024-T3 aluminium alloy, Corros. Sci. 155 (2019) 109–120.

[13] S. Akbarzadeh, L. Sopchenski Santos, V. Vitry, Y. Paint, M.G. Olivier, Improvement of the corrosion performance of AA2024 alloy by a duplex PEO/clay modified sol-gel nanocomposite coating, Surf. Coat. Technol. 434 (2022), 128168.

[14] R. del Olmo, M. Mohedano, P. Visser, E. Matykina, R. Arrabal, Flash-PEO coatings loaded with corrosion inhibitors on AA2024, Surf. Coat. Technol. 402 (2020), 126317.

[15] R. Arrabal, M. Mohedano, E. Matykina, A. Pardo, B. Mingo, M.C. Merino, Characterization and wear behaviour of PEO coatings on 6082-T6 aluminium alloy with incorporated α-Al2O3 particles, Surf. Coat. Technol. 269 (2015) 64–73.

[16] P. Molaeipour, S.R. Allahkaram, S. Akbarzadeh, Corrosion inhibition of Ti6Al4V alloy by a protective plasma electrolytic oxidation coating modified with boron carbide nanoparticles, Surf. Coat. Technol. 430 (2022), 127987.

[17] B. Mingo, Y. Guo, A. Němcová, A. Gholinia, M. Mohedano, M. Sun, A. Matthews, A. Yerokhin, Incorporation of halloysite nanotubes into forsterite surface layer during plasma electrolytic oxidation of AM50 Mg alloy, Electrochim. Acta 299 (2019) 772–788.

[18] B. Hamrahi, B. Yarmand, A. Massoudi, Improved in-vitro corrosion performance of titanium using a duplex system of plasma electrolytic oxidation and graphene oxide incorporated silane coatings, Surf. Coatings Technol 422 (2021), 127558.

[19] G. Peitao, T. Mingyang, Z. Chaoyang, Tribological and corrosion resistance properties of graphite composite coating on AZ31 Mg alloy surface produced by plasma electrolytic oxidation, Surf. Coat. Technol. 359 (2019) 197–205.

[20] H. Jun Xie, Y. Liang Cheng, S. Xian Li, J. Hui Cao, L. Cao, Wear and corrosion resistant coatings on surface of cast A356 aluminum alloy by plasma electrolytic oxidation in moderately concentrated aluminate electrolytes, Trans. Nonferrous Met. Soc. China 27 (2017) 336–351.

[21] K. Li, W. Li, G. Zhang, W. Zhu, F. Zheng, D. Zhang, M. Wang, Effects of Si phase refinement on the plasma electrolytic oxidation of eutectic Al-Si alloy, J. Alloy. Compd. 790 (2019) 650–656.

[22] L. Wang, L. Chen, Z. Yan, W. Fu, Optical emission spectroscopy studies of discharge mechanism and plasma characteristics during plasma electrolytic oxidation of magnesium in different electrolytes, Surf. Coat. Technol. 205 (2010) 1651–1658.

[23] L.O. Snizhko, A.L. Yerokhin, A. Pilkington, N.L. Gurevina, D.O. Misnyankin, A. Leyland, A. Matthews, Anodic processes in plasma electrolytic oxidation of aluminium in alkaline solutions, Electrochim. Acta 49 (2004) 2085–2095.

[24] M. Treviño, R.D. Mercado-Solis, R. Colás, A. Pérez, J. Talamantes, A. Velasco, Erosive wear of plasma electrolytic oxidation layers on aluminium alloy 6061, Wear 301 (2013) 434–441.

[25] L. Pezzato, R. Babbolin, P. Cerchier, M. Marigo, P. Dolcet, M. Dabalà, K. Brunelli, Sealing of PEO coated AZ91magnesium alloy using solutions containing neodymium, Corros. Sci. 173 (2020), 108741.

[26] J. Joo, D. Kim, H.S. Moon, K. Kim, J. Lee, Durable anti-corrosive oil-impregnated porous surface of magnesium alloy by plasma electrolytic oxidation with hydrothermal treatment, Appl. Surf. Sci. 509 (2020), 145361.

[27] D.V. Mashtalyar, K.V. Nadaraia, I.M. Imshinetskiy, E.A. Belov, V.S. Filonina, S. N. Suchkov, S.L. Sinebryukhov, S.V. Gnedenkov, Composite coatings formed on Ti by PEO and fluoropolymer treatment, Appl. Surf. Sci. 536 (2021), 147976.

[28] S. Akbarzadeh, M. Ramezanzadeh, B. Ramezanzadeh, M. Mahdavian, R. Naderi, Fabrication of highly effective polyaniline grafted carbon nanotubes to induce active protective functioning in a silane coating, Ind. Eng. Chem. Res. 58 (2019) 20309–20322.

[29] A. Mehner, H.W. Zoch, W. Datchary, G. Pongs, Sol-gel coatings for high precision optical molds, CIRP Ann. 55 (2006) 589–592.

[30] S. Akbarzadeh, K. Akbarzadeh, M. Ramezanzadeh, R. Naderi, M. Mahdavian, M. G. Olivier, Corrosion resistance enhancement of a sol-gel coating by incorporation of modified carbon nanotubes: Artificial neural network (ANN) modeling and experimental explorations, Prog. Org. Coat. 174 (2023), 107296.

[31] J.D. Mackenzie, E.P. Bescher, Physical properties of sol-gel coatings, J. Sol. Gel Sci. Technol. 19 (2000) 23–29.

[32] S. Akbarzadeh, R. Naderi, M. Mahdavian, Fabrication of a highly protective silane composite coating with limited water uptake utilizing functionalized carbon nano-tubes, Compos. Part B Eng. 175 (2019), 107109.

[33] C. Wang, J. Shen, X. Zhang, B. Duan, J. Sang, In vitro degradation and cytocompatibility of a silane/Mg(OH)2 composite coating on AZ31 alloy by spin coating, J. Alloy. Compd. 714 (2017) 186–193.

[34] S. Nezamdoust, D. Seifzadeh, Application of CeH–V/ sol–gel composite coating for corrosion protection of AM60B magnesium alloy, Trans. Nonferrous Met. Soc. China 27 (2017) 352–362.

[35] J. Hu, D. Zeng, Z. Zhang, T. Shi, G.L. Song, X. Guo, 2-Hydroxy-4-methoxy-acetophenone as an environment-friendly corrosion inhibitor for AZ91D magnesium alloy, Corros. Sci. 74 (2013) 35–43.

[36] N. Dinodi, A.N. Shetty, Alkyl carboxylates as efficient and green inhibitors of magnesium alloy ZE41 corrosion in aqueous salt solution, Corros. Sci. 85 (2014) 411–427.

[37] I.A. Kartsonakis, S.G. Stanciu, A.A. Matei, E.K. Karaxi, R. Hristu, A. Karantonis, C. A. Charitidis, Evaluation of the protective ability of typical corrosion inhibitors for magnesium alloys towards the Mg ZK30 variant, Corros. Sci. 100 (2015) 194–208.

[38] X. Lu, Y. Li, P. Ju, Y. Chen, J. Yang, K. Qian, T. Zhang, F. Wang, Unveiling the inhibition mechanism of an effective inhibitor for AZ91 Mg alloy, Corros. Sci. 148 (2019) 264–271.

[39] M. Sun, A. Yerokhin, M.Y. Bychkova, D.V. Shtansky, E.A. Levashov, A. Matthews, Self-healing plasma electrolytic oxidation coatings doped with benzotriazole loaded halloysite nanotubes on AM50 magnesium alloy, Corros. Sci. 111 (2016) 753–769.

[40] S.V. Lamaka, D. Knörnschild, D.V. Snihirova, M.G. Taryba, M.L. Zheludkevich, M. G.S. Ferreira, Complex anticorrosion coating for ZK30 magnesium alloy, Electrochim. Acta 55 (2009) 131–141.

[41] J. Yang, C. Blawert, S.V. Lamaka, D. Snihirova, X. Lu, S. Di, M.L. Zheludkevich, Corrosion protection properties of inhibitor containing hybrid PEO-epoxy coating on magnesium, Corros. Sci. 140 (2018) 99–110.

[42] A.S. Gnedenkov, S.L. Sinebryukhov, D.V. Mashtalyar, S.V. Gnedenkov, Protective properties of inhibitor-containing composite coatings on a Mg alloy, Corros. Sci. 102 (2016) 348–354.

[43] A.S. Gnedenkov, S.L. Sinebryukhov, D.V. Mashtalyar, S.V. Gnedenkov, Localized corrosion of the Mg alloys with inhibitor-containing coatings: SVET and SIET studies, Corros. Sci. 102 (2016) 269–278.

[44] M. Mohedano, C. Blawert, M.L. Zheludkevich, Cerium-based sealing of PEO coated AM50 magnesium alloy, Surf. Coat. Technol. 269 (2015) 145–154.

[45] D.K. Ivanou, M. Starykevich, A.D. Lisenkov, M.L. Zheludkevich, H.B. Xue, S. V. Lamaka, M.G.S. Ferreira, Plasma anodized ZE41 magnesium alloy sealed with hybrid epoxy-silane coating, Corros. Sci. 73 (2013) 300–308.

[46] K.A. Yasakau, M.L. Zheludkevich, O.V. Karavai, M.G.S. Ferreira, Influence of inhibitor addition on the corrosion protection performance of sol–gel coatings on AA2024, Prog. Org. Coat. 63 (2008) 352–361.

[47] S.V. Lamaka, M.L. Zheludkevich, K.A. Yasakau, M.F. Montemor, M.G.S. Ferreira, High effective organic corrosion inhibitors for 2024 aluminium alloy, Electrochim. Acta 52 (2007) 7231–7247.

[48] I.A. Kartsonakis, E. Athanasopoulou, D. Snihirova, B. Martins, M.A. Koklioti, M. F. Montemor, G. Kordas, C.A. Charitidis, Multifunctional epoxy coatings combining a mixture of traps and inhibitor loaded nanocontainers for corrosion protection of AA2024-T3, Corros. Sci. 85 (2014) 147–159.

[49] L.B. Coelho, M. Mouanga, M.E. Druart, I. Recloux, D. Cossement, M.G. Olivier, A SVET study of the inhibitive effects of benzotriazole and cerium chloride solely and combined on an aluminium/copper galvanic coupling model, Corros. Sci. 110 (2016) 143–156.

[50] I. Recloux, F. Andreatta, M.E. Druart, L.B. Coelho, C. Cepek, D. Cossement, L. Fedrizzi, M.G. Olivier, Stability of benzotriazole-based films against AA2024 aluminium alloy corrosion process in neutral chloride electrolyte, J. Alloy. Compd. 735 (2018) 2512–2522.

[51] L. Garrigues, N. Pebere, F. Dabosi, An investigation of the corrosion inhibition of pure aluminum in neutral and acidic chloride solutions, Electrochim. Acta 41 (1996) 1209–1215.

[52] G.P. Cicileo, B.M. Rosales, F.E. Varela, J.R. Vilche, Inhibitory action of 8-HYDROXYQUINOLINE on the copper corrosion process, Corros. Sci. 40 (1998) 1915–1926.

[53] K. Aramaki, T. Kiuchi, T. Sumiyoshi, H. Nishihara, Surface enhanced Raman scattering and impedance studies on the inhibition of copper corrosion in sulphate solutions by 5-substituted benzotriazoles, Corros. Sci. 32 (1991) 593–607.

[54] I. Milošev, B. Kapun, P. Rodič, J. Iskra, Hybrid sol–gel coating agents based on zirconium(IV) propoxide and epoxysilane, J. Sol. Gel Sci. Technol. 74 (2015) 447–459.

[55] L. Sopchenski, J. Robert, M. Touzin, A. Tricoteaux, M.G. Olivier, Improvement of wear and corrosion protection of PEO on AA2024 via sol-gel sealing, Surf. Coat. Technol. 417 (2021), 127195.

[56] H. Costenaro, A. Lanzutti, Y. Paint, L. Fedrizzi, M. Terada, H.G. de Melo, M.G. Olivier, Corrosion resistance of 2524 Al alloy anodized in tartaric-sulphuric acid at different voltages and protected with a TEOS-GPTMS hybrid sol-gel coating, Surf. Coat. Technol. 324 (2017) 438–450.

[57] P. Molaeipour, M. Ramezanzadeh, B. Ramezanzadeh, Stachys byzantina extract: A green biocompatible molecules source for graphene skeletons generation on the carbon steel for superior corrosion mitigation, Bioelectrochemistry 143 (2022), 107970.

[58] S. Akbarzadeh, M. Ramezanzadeh, B. Ramezanzadeh, G. Bahlakeh, Detailed atomic/molecular-level/electronic-scale computer modeling and electrochemical explorations of the adsorption and anti-corrosion effectiveness of the green nitrogen-based phytochemicals on the mild steel surface in the saline solution, J. Mol. Liq. 319 (2020), 114312.

[59] C.L. Alexander, B. Tribollet, M.E. Orazem, Contribution of surface distributions to constant-phase-element (CPE) behavior: 1. influence of roughness, Electrochim. Acta 173 (2015) 416–424.

[60] M. Serdechnova, M. Mohedano, B. Kuznetsov, C.L. Mendis, M. Starykevich, S. Karpushenkov, J. Tedim, M.G.S. Ferreira, C. Blawert, M.L. Zheludkevich, PEO coatings with active protection based on in-situ formed LDH-nanocontainers, J. Electrochem. Soc. 164 (2017) C36–C45.

[61] R.O. Hussein, X. Nie, D.O. Northwood, A. Yerokhin, A. Matthews, Spectroscopic study of electrolytic plasma and discharging behaviour during the plasma electrolytic oxidation (PEO) process, J. Phys. D Appl. Phys. 43 (2010), 105203.

[62] R.H.U. Khan, A. Yerokhin, X. Li, H. Dong, A. Matthews, Surface characterisation of DC plasma electrolytic oxidation treated 6082 aluminium alloy: Effect of current density and electrolyte concentration, Surf. Coat. Technol. 205 (2010) 1679–1688.

[63] W. Xue, Z. Deng, Y. Lai, R. Chen, Analysis of phase distribution for ceramic coatings formed by microarc oxidation on aluminum alloy, J. Am. Ceram. Soc. 81 (1998) 1365–1368.

[64] N.C. Rosero-Navarro, S.A. Pellice, Y. Castro, M. Aparicio, A. Durán, Improved corrosion resistance of AA2024 alloys through hybrid organic–inorganic sol–gel coatings produced from sols with controlled polymerisation, Surf. Coat. Technol. 203 (2009) 1897–1903.

[65] K. Studer, C. Decker, E. Beck, R. Schwalm, Overcoming oxygen inhibition in UV-curing of acrylate coatings by carbon dioxide inerting: Part II, Prog. Org. Coat. 48 (2003) 101–111.

[66] B. Ramezanzadeh, Z. Haeri, M. Ramezanzadeh, A facile route of making silica nanoparticles-covered graphene oxide nanohybrids (SiO2-GO); fabrication of SiO2-GO/epoxy composite coating with superior barrier and corrosion protection performance, Chem. Eng. J. 303 (2016) 511–528.

[67] V. Tagliazucca, E. Callone, S. Dirè, Influence of synthesis conditions on the cross-link architecture of silsesquioxanes prepared by in situ water production route, J. Sol. Gel Sci. Technol. 60 (2011) 236–245.

[68] A.F. Galio, S.V. Lamaka, M.L. Zheludkevich, L.F.P. Dick, I.L. Müller, M.G.S. Ferreira, Inhibitor-doped sol–gel coatings for corrosion protection of magnesium alloy AZ31, Surf. Coat. Technol. 204 (2010) 1479–1486.

[69] S.L. Hruby, B.H. Shanks, Acid–base cooperativity in condensation reactions with functionalized mesoporous silica catalysts, J. Catal. 263 (2009) 181–188.

[70] O. Paquet, M.C.B. Salon, E. Zeno, M.N. Belgacem, Hydrolysis-condensation kinetics of 3-(2-amino-ethylamino)propyl-trimethoxysilane, Mater. Sci. Eng. C 32 (2012) 487–493.

[71] P.G. Fox, G. Lewis, P.J. Boden, Some chemical aspects of the corrosion inhibition of copper by benztriazole, Corros. Sci. 19 (1979) 457–467.

[72] R.F. Roberts, X-ray photoelectron spectroscopic characterization of copper oxide surfaces treated with benzotriazole, J. Electron Spectrosc. Relat. Phenom. 4 (1974) 273–291.

[73] H. Gerengi, M.M. Solomon, M. Kurtay, G. Bereket, K. Goksen, M. Yıldız, E. Kaya, Electrochemical and morphological assessments of inhibition level of 8-hydroxyl-quinoline for AA2024-T4 alloy in 3.5% NaCl solution, J. Adhes. Sci. Technol. 32 (2018) 207–223.

[74] L. Tang, X. Li, Y. Si, G. Mu, G. Liu, The synergistic inhibition between 8-hydroxyquinoline and chloride ion for the corrosion of cold rolled steel in 0.5 M sulfuric acid, Mater. Chem. Phys. 95 (2006) 29–38.

[75] S. Marcelin, N. Pébère, Synergistic effect between 8-hydroxyquinoline and benzotriazole for the corrosion protection of 2024 aluminium alloy: A local electrochemical impedance approach, Corros. Sci. 101 (2015) 66–74.

[76] S. Akbarzadeh, Y. Paint, M.-G. Olivier, A comparative study of different sol-gel coatings for sealing the plasma electrolytic oxidation (PEO) layer on AA2024 alloy, Electrochim. Acta 443 (2023), 141930.

[77] G. Rosace, E. Guido, C. Colleoni, G. Barigozzi, Influence of textile structure and silica based finishing on thermal insulation properties of cotton fabrics, Int. J. Polym. Sci. 2016 (2016).

[78] M.V. Reyes-Peces, A. Pérez-Moreno, D.M. De-Los-santos, M.D.M. Mesa-Díaz, G. Pinaglia-Tobaruela, J.I. Vilches-Pérez, R. Fernández-Montesinos, M. Salido, N. de la Rosa-Fox, M. Piñero, Chitosan-GPTMS-silica hybrid mesoporous aerogels for bone tissue engineering, Polymers 12 (2020) 2723.

[79] D.K. Ivanou, K.A. Yasakau, S. Kallip, A.D. Lisenkov, M. Starykevich, S.V. Lamaka, M.G.S. Ferreira, M.L. Zheludkevich, Active corrosion protection coating for a ZE41 magnesium alloy created by combining PEO and sol–gel techniques, RSC Adv. 6 (2016) 12553–12560.

[80] W. Liu, Y. Pu, H. Liao, Y. Lin, W. He, Corrosion and wear behavior of PEO coatings on D16T aluminum alloy with different concentrations of graphene, Coatings 10 (2020) 249.

[81] M. Zhu, Y. Song, K. Dong, D. Shan, E.H. Han, Correlation between the transient variation in positive/negative pulse voltages and the growth of PEO coating on 7075 aluminum alloy, Electrochim. Acta 411 (2022), 140056.

[82] S. Amand, M. Musiani, M.E. Orazem, N. Pébère, B. Tribollet, V. Vivier, Constant-phase-element behavior caused by inhomogeneous water uptake in anti-corrosion coatings, Electrochim. Acta 87 (2013) 693–700.

[83] H.H. Hernández, A.M.R. Reynoso, J.C.T. González, C.O.G. Morán, J.G.M. Hernández, A.M. Ruiz, J.M. Hernández, R.O. Cruz, Electrochemical impedance spectroscopy (EIS): a review study of basic aspects of the corrosion mechanism applied to steels, Electrochem. Impedance Spectrosc. (2020).

[84] S. Akbarzadeh, M. Ramezanzadeh, B. Ramezanzadeh, G. Bahlakeh, A green assisted route for the fabrication of a high-efficiency self-healing anti-corrosion coating through graphene oxide nanoplatform reduction by Tamarindus indiaca extract, J. Hazard. Mater. 390 (2020), 122147.

[85] S. Akbarzadeh, M. Ramezanzadeh, B. Ramezanzadeh, Inspection the corrosion prevention performance and dry/wet interfacial adhesion qualities of the melamine-cured polyester coating applied on the treated mild steel surface with a nanostructured composite cerium-neodymium film, Colloids Surf. A Physicochem. Eng. Asp. 590 (2020), 124472.

[86] L. Pezzato, M. Rigon, A. Martucci, K. Brunelli, M. Dabalà, Plasma Electrolytic Oxidation (PEO) as pre-treatment for sol-gel coating on aluminum and magnesium alloys, Surf. Coat. Technol. 366 (2019) 114–123.

[87] M. Arunoday, K.P. Premkumar, R. Kumar, R. Subasri, Multifunctional, environmental coatings on AA2024 by combining anodization with sol-gel process, Ceram. Int. 48 (2022) 10969–10978.

[88] Y. Chen, X. Lu, S.V. Lamaka, P. Ju, C. Blawert, T. Zhang, F. Wang, M.L. Zheludkevich, Active protection of Mg alloy by composite PEO coating loaded with corrosion inhibitors, Appl. Surf. Sci. 504 (2020), 144462.

[89] L. Pezzato, L.B. Coelho, R. Bertolini, A.G. Settimi, K. Brunelli, M. Olivier, M. Dabalà, Corrosion and mechanical properties of plasma electrolytic oxidation-coated AZ80 magnesium alloy, Mater. Corros. 70 (2019) 2103–2112.

[90] N. Dimitrov, J.A. Mann, M. Vukmirovic, K. Sieradzki, Dealloying of Al2CuMg in alkaline media, J. Electrochem. Soc. 147 (2000) 3283.

[91] M.L. Zheludkevich, K.A. Yasakau, S.K. Poznyak, M.G.S. Ferreira, Triazole and thiazole derivatives as corrosion inhibitors for AA2024 aluminium alloy, Corros. Sci. 47 (2005) 3368–3383.

[92] C. Casenave, N. Pebere, F. Dabosi, An electrochemical impedance study of the corrosion inhibition of a 2024 aluminum alloy in neutral chloride solutions, Mater. Sci. Forum 192–194 (1995) 599–610.

[93] D. Fix, D.V. Andreeva, Y.M. Lvov, D.G. Shchukin, H. Möhwald, Application of inhibitor-loaded halloysite nanotubes in active anti-corrosive coatings, Adv. Funct. Mater. 19 (2009) 1720–1727.